



Science Arts & Métiers (SAM)

is an open access repository that collects the work of Arts et Métiers Institute of Technology researchers and makes it freely available over the web where possible.

This is an author-deposited version published in: <https://sam.ensam.eu>
Handle ID: <http://hdl.handle.net/10985/15356>

To cite this version :

Marta BERARDENGO, Stefano MANZONI, Olivier THOMAS, Marcello VANALI - Piezoelectric resonant shunt enhancement by negative capacitances: Optimisation, performance and resonance cancellation - Journal of Intelligent Material Systems and Structures - Vol. 29, n°12, p.2581-2606 - 2018

Any correspondence concerning this service should be sent to the repository

Administrator : scienceouverte@ensam.eu



Piezoelectric resonant shunt enhancement by negative capacitances: Optimisation, performance and resonance cancellation

Marta Berardengo¹, Stefano Manzoni², Olivier Thomas³
and Marcello Vanali¹

Abstract

This article addresses piezoelectric shunt damping through a resonant shunt associated with negative capacitances. The main objective of this article is to provide guidelines for choosing the best electrical circuit layout in terms of control performance and possible stability issues. This article proposes general analytical formulations for the tuning/optimisation of the electrical shunt impedance and for the prediction of the attenuation performance. These formulations are demonstrated to be valid for all the possible configurations of the negative capacitances. It is demonstrated that the behaviour of the different shunt circuits can indeed be described by a common mathematical treatment. Moreover, the use of two negative capacitances together is shown to provide benefits compared to traditional layouts based on a single negative capacitance. The mentioned advantages relate to both stability and attenuation performance. The use of a resonant shunt with the addition of negative capacitances is finally proven to provide enough attenuation to even cancel eigenfrequency peaks in some cases. This article also analyses the main issues arising from the practical implementation of the negative capacitances. Finally, the theoretical results are validated through experiments conducted on a cantilever beam coupled to two piezoelectric patches.

Keywords

Piezoelectric shunt, resonant shunt, negative capacitance, damping, vibration control

Introduction

Piezoelectric shunt is a well-known technique for vibration damping. This approach relies on the electrical link between a piezoelectric actuator, bonded to a vibrating structure, and a properly designed electrical network (Hagood and Von Flotow, 1991). The most used shunt impedances for single-mode control are a simple resistance (resistive shunt or R-shunt) and the series of a resistance and an inductance (resonant shunt or LR-shunt; Hagood and Von Flotow, 1991; Thomas et al., 2012; Yamada et al., 2010).

Thomas et al. (2009, 2012) and Ducarne et al. (2012) demonstrated that as soon as the electric impedance is optimally tuned, the performance of the control depends only on the modal electromechanical coupling factor (MEMCF) of each mode of the electromechanical system (EMS; composed of the vibrating structure, the piezoelectric actuator and the shunt impedance).

The MEMCF is a feature of the EMS, and it is a function of the mechanical, geometrical, and electrical characteristics of the structure and the piezoelectric actuator. The MEMCF of a given mode is proven to also be related to the distance between the natural frequencies of the EMS in short circuit (SC) and open circuit (OC) of the mode considered. The higher the MEMCF is, the higher the maximum achievable attenuation is (Thomas et al., 2012).

The use of synthetic circuits can improve the attenuation performance provided by the optimally tuned shunt (e.g. Date et al., 2000; Sluka and Mokry, 2007; Tang and Wang, 2001). Among these circuits, the use of negative capacitances (NCs) has been shown to be highly reliable and effective in enhancing the performance of piezoelectric shunt damping. NCs do not exist in nature, but they can be implemented by using operational amplifiers (OP-AMPs) (Horowitz and Hill, 1989). NCs were fruitfully employed coupled to a resistive shunt (Beck et al., 2013, 2014; Behrens et al., 2003; Berardengo et al., 2016b, 2017; Collet et al., 2011; De Marneffe and Preumont, 2008; Kodejška et al., 2012; Manzoni et al., 2012; Park and Baz, 2005) and to a resonant shunt (De Marneffe and Preumont, 2008; Heuss et al., 2016; Neubauer et al., 2006). The resonant shunt coupled to NCs was proven to be highly effective in reducing the vibration level when single-mode control is needed. Furthermore, its attenuation performance is higher than that of the resistive shunt coupled to NCs. For this reason, the study of this shunt circuit deserves attention from the scientific community.

This article specifically addresses the coupling between NCs and a resonant shunt; thus, it is worth explaining the main content of the referenced works related to this type of damping approach. De Marneffe and Preumont (2008) analysed the damping performance provided by this type of shunt compared to other approaches; among them, active control was also considered. The coupling between a resonant shunt and NCs resulted in among the best solutions for the attenuation of vibrations, showing very good performance. Neubauer et al. (2006) proposed optimisation criteria for a shunt composed of a series connection of an NC, a resistance and an inductance. Heuss et al. (2016) used the connection of an NC and a resonant shunt to develop a vibration absorber composed of a beam and a piezoelectric patch connected to the mentioned shunt impedance.

However, there are still many open issues regarding the coupling between NCs and resonant shunts. The aim of this article is to address these open issues by exploiting a mathematical approach that has already been successfully used by the authors to describe the coupling between NCs and resistive shunts (Berardengo et al., 2015b, 2016b, 2017).

Specifically, this article addresses the following points:

1. It shows that it is possible to find a common mathematical treatment that is valid for all the possible connection types of NCs with a resonant shunt, which was not previously demonstrated in the literature;
2. It provides a comparison of the damping performance of the different possible layouts of the electrical network, which is currently lacking in

the literature. This comparison also allows demonstrating that it is possible to reach resonance cancellation in specific operating conditions, thus revealing the high damping performance offered by NCs coupled to a resonant shunt;

3. It discusses the effect of the practical implementation of NCs, which is generally neglected in the literature. Indeed, an issue related to the use of NCs is that the simplest circuit layouts employed to construct the NCs, named ideal circuits (ICs) here, occasionally cannot be used in practice. In such cases, more complex circuits, named real circuits (RCs) here, must be used because they are more reliable for a practical implementation. Unlike the ICs, the RCs cannot be considered as pure NCs (see later in this article, that is, the section related to the effects of the NC implementation on system stability and damping performance) but rather as complex negative impedances. Here, the aim is not to explain how to modify ICs to achieve RC configurations, which is already explained in the literature (e.g. Beck et al., 2013; Moheimani and Fleming, 2006), but rather to show the effects of RCs coupled to a resonant shunt in terms of damping performance and EMS stability. Moreover, related to this point, the stability analysis of a complex multi-degrees-of-freedom structure when an RC NC is coupled to a resonant shunt is discussed because it has never been addressed in the literature. Indeed, note that the active nature of the NC circuit poses some issues related to EMS stability, and thus, stability must always be studied.

Regarding the first point of the above list, recall that a piezoelectric actuator can be linked to a passive shunt impedance Z_{sh} and NCs in three different ways: parallel, series and series + parallel (SP) (Berardengo et al., 2015b, 2016b, 2017), as explained in Figure 1(a) to (c) ($-C_1$ denotes the IC NC in the parallel configuration, while $-C_2$ denotes the IC NC connected in series). The theoretical approach presented in Berardengo et al. (2016b, 2017) can be fruitfully exploited to show that a common mathematical description can also be derived for the coupling between IC NCs and the resonant shunt, regardless of the type of NC connection used. This allows presenting brand-new formulations for the optimisation of the shunt impedance and for the prediction of the attenuation. Furthermore, the coupling between the resonant shunt and NCs in the SP configuration will be treated herein, which has not previously been considered in the literature. This new general formulation thus makes the comparison of the different shunt layouts in terms of damping

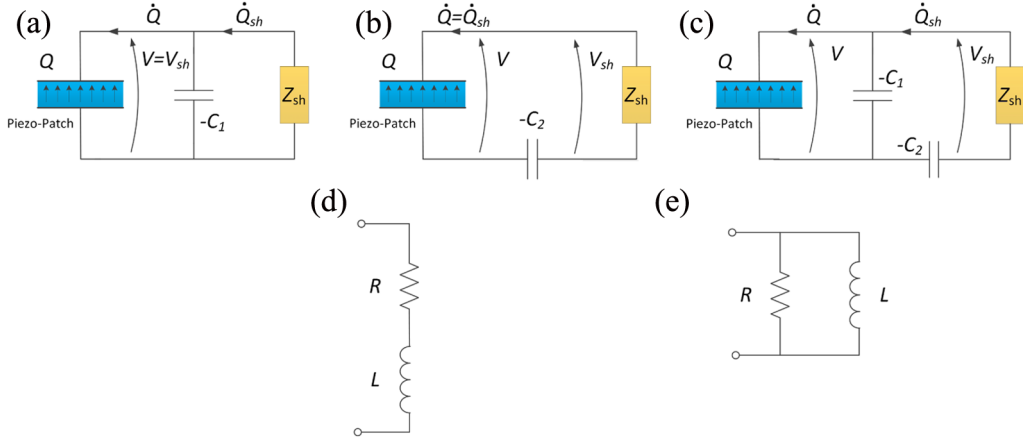


Figure 1. Piezoelectric shunt with NCs: (a) parallel, (b) series and (c) SP configurations; Z_{sh} is a passive shunt impedance. When a resonant shunt is considered, this impedance Z_{sh} is made from an inductance L and a resistance R connected in either (d) series or (e) parallel. Refer to the main text of the section entitled ‘Coupling of an NC with an arbitrary impedance’ for the definitions of the other symbols in the figure.

performance possible and straightforward, thereby filling the gap related to point 2 of the above list. This comparison will prove the possibility of achieving resonance cancellation in given operating conditions. Regarding point 3 of the list, the effects of using RC NCs in place of IC NCs on both the attenuation performance and the stability are taken into account and described herein. This will allow for a complete comparison of all the possible shunt layouts.

All the mentioned analyses will allow developing guidelines for how to apply shunt damping by coupling NCs and resonant circuits. These guidelines aim to explain the best layout to be used for a specific case and how to enhance the stability of the EMS.

Therefore, this article uses a mathematical approach previously developed to describe shunt damping through NCs coupled to a resistive shunt to describe the damping offered by NCs coupled to a resonant shunt. This allows the authors to reveal many features of this specific damping approach, as explained in the previous list.

The remainder of this article is structured as follows. The next section describes the theoretical model employed in this article. The subsequent section analyses the stability of the EMS when coupled to IC NCs and provides the analytical expressions to be used for optimising the values of the elements of the shunt impedance, as well as the expressions of the associated vibration attenuation. Then, the article shows the effect of using RC NCs and provides the mentioned guidelines for using NCs coupled to a resonant shunt. Finally, the last section of the article describes the experiments conducted to validate the theoretical results.

Model of the EMS

Coupling of an NC with an arbitrary impedance

The model used here was originally developed in the works of Thomas et al. (2009, 2012) and Ducarne et al. (2012) and then improved in the works of Berardengo et al. (2016b, 2017), where a deeper insight into the electrical behaviour of the EMS enables a better description of the system dynamics, thereby improving the accuracy of the original model. Only the parts of the model that are fundamental for a deep understanding of the article are reported in this section. Readers can refer to the referenced works for a detailed description of the model. From the next subsection (i.e. the subsection related to the coupling between a resonant shunt and NCs) on, the new outcomes related to the coupling between NCs and a resonant shunt are addressed.

A generic elastic structure with one piezoelectric patch bonded on it and excited by an external force F_{ext} is considered (see Figure 2). A generic passive shunt impedance Z is connected to the piezoelectric patch, V is the voltage between the electrodes of the piezoelectric actuator, Q is the electric charge in one of the electrodes, and considering the sign convention for

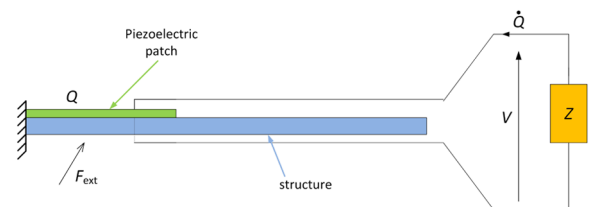


Figure 2. An arbitrary structure with a piezoelectric patch connected to a passive shunt impedance Z .

V in Figure 2, Q is precisely the charge in the upper electrode. A reduced-order model of the EMS can be obtained by expressing the displacement of any point x of the structure at time t , $U(x, t)$, in modal coordinates and considering N vibration eigenmodes (N being infinite in theory)

$$U(x, t) = \sum_{i=1}^N \Phi_i(x) q_i(t) \quad (1)$$

where Φ_i is the i th eigenmode of the structure (normalised to the unit modal mass) and q_i is the i th modal coordinate. Note that even if the structure shown in Figure 2 is a cantilever beam, any type of structure can be considered, and the discussion is still valid, thanks to its general formulation. Therefore, the displacement U can be in any direction, and x is intended to be a generic coordinate defining the position over the structure.

In the case of low modal density and if a single-degree-of-freedom (SDOF) approximation is considered by keeping only the i th mode in the modal truncation, the behaviour of the EMS can be described for $\Omega \simeq \omega_i$ (where Ω is the angular frequency) as follows

$$\ddot{q}_i + 2\xi_i \omega_i \dot{q}_i + \omega_i^2 q_i - \chi_i V = F_i \quad (2)$$

$$C_{pi} V - Q + \chi_i q_i = 0 \quad (3)$$

where equation (2) is the equation of motion of the EMS, and it is coupled to the EMS electrical behaviour, described by equation (3), through the coefficient χ_i . F_i is the modal forcing, which depends on F_{ext} and the i th mode shape Φ_i . Note that Φ_i are the eigenmodes of the EMS with the piezoelectric patch in SC (with $V = 0$). ω_i is the i th natural frequency of the EMS in SC, ξ_i is the associated structural damping factor, and χ_i is a modal coupling coefficient, which is related to the energy transfer between the i th mode shape and the piezoelectric patch. The values of χ_i are functions of the mechanical, geometrical and electrical characteristics of the piezoelectric actuator and the structure, as well as of the position of the actuator. It is possible to compute the χ_i coefficients either analytically (Ducarne et al., 2012) or using a finite element model (Thomas et al., 2009); an alternative approach is to estimate the χ_i coefficients experimentally, as explained at the end of this section.

The term C_{pi} in equation (3) is the value of the capacitance of the piezoelectric patch at frequencies above ω_i when an SDOF approximation is performed on the complete model (Berardengo et al., 2016b), and it is defined as follows

$$C_{pi} = C_\infty + \sum_{n=i+1}^N \frac{\chi_n^2}{\omega_n^2} \quad \forall i = 1, \dots, N-1 \quad (4)$$

where C_∞ is the electrical blocked capacitance of the piezoelectric patch (i.e. the capacitance value with

$U(x, t) = 0 \quad \forall x \Rightarrow q_i = 0 \quad \forall i$). The second term on the right-hand side of equation (4) accounts for the contribution to the capacitance value of the modes higher than the i th mode, which are neglected in the SDOF approximation. This static correction, introduced in Berardengo et al. (2016b), is an improvement to the model proposed in Thomas et al. (2012) and enables achieving a more accurate description of the EMS when an SDOF approximation is considered. The value of C_{pi} can be estimated by measuring the capacitance of the piezoelectric patch at a frequency between the i th and $(i+1)$ th modes. A more refined approach to estimate the C_{pi} value is to measure the piezoelectric capacitance at several frequency values and then update the model of the piezoelectric capacitance using the acquired data, as explained in Appendix 1. Moreover, details about the definition of C_{pi} and its estimation can also be found in Berardengo et al. (2016b).

The model described by equations (2) and (3) is related to the case of a simple piezoelectric shunt where no NCs are included in the circuit. The addition of IC NCs is now addressed according to the network layouts described by the schemes in Figure 1(a) to (c). RC NCs will be considered later in this article (i.e. in the section related to the effects of the NC implementation on system stability and damping performance). The passive shunt impedance in the circuit without NCs was referred to as Z in Figure 2. Conversely, the passive shunt impedance is referred to as Z_{sh} in Figure 1(a) to (c), where NCs are added to the circuit. This difference in nomenclature helps to differentiate the two different situations considered: the absence or presence of NCs.

The following change in variables is now introduced

$$\bar{V}_{\text{sh}} = V_{\text{sh}} \sqrt{C_{\text{eq}}}, \quad \bar{Q}_{\text{sh}} = \frac{Q_{\text{sh}}}{\sqrt{C_{\text{eq}}}} \quad (5)$$

here, Q_{sh} and V_{sh} are the charge and the voltage seen by the shunt impedance Z_{sh} (see Figure 1(a) to (c)), respectively. C_{eq} is an equivalent capacitance, defined in Table 1. This equivalent capacitance depends on the IC NCs connected to the piezoelectric patch, and thus, it depends on the type of NC layout (parallel, series or SP; see Figure 1(a) to (c)). According to Berardengo et al. (2016b), the following system of equations is obtained using equation (5)

$$\ddot{q}_i + 2\xi_i \omega_i \dot{q}_i + (\omega_i^{\text{sc}})^2 q_i - \omega_i \tilde{k}_i \bar{V}_{\text{sh}} = F_i \quad (6)$$

$$\ddot{q}_i + 2\xi_i \omega_i \dot{q}_i + (\omega_i^{\text{sc}})^2 q_i - \omega_i \tilde{k}_i \bar{Q}_{\text{sh}} = F_i \quad (7)$$

$$\bar{V}_{\text{sh}} - \bar{Q}_{\text{sh}} + \omega_i \tilde{k}_i q_i = 0 \quad (8)$$

Equations (6) to (8) describe the electromechanical behaviour of the EMS when NCs are added in the electric circuit. These equations play the same role as equations (2) and (3): the latter are related to an EMS without NCs, whereas the former are related to an

Table 1. Parameters of the EMS without NCs, enhanced by a single NC in parallel and series configurations and enhanced by two NCs for the SP configuration.

	Simple shunt without NCs	Parallel configuration	Series configuration	SP configuration
$\omega_i^{\text{sc}} =$	ω_i	ω_i	$\sqrt{\omega_i^2 - \frac{\chi_i^2}{C_2 - C_{pi}}}$	$\sqrt{\omega_i^2 - \frac{\chi_i^2}{C_1 + C_2 - C_{pi}}}$
$\omega_i^{\text{oc}} =$	$\hat{\omega}_i = \sqrt{\omega_i^2 + \frac{\chi_i^2}{C_{pi}}}$	$\sqrt{\omega_i^2 + \frac{\chi_i^2}{C_{pi} - C_1}}$	$\hat{\omega}_i = \sqrt{\omega_i^2 + \frac{\chi_i^2}{C_{pi}}}$	$\sqrt{\omega_i^2 + \frac{\chi_i^2}{C_{pi} - C_1}}$
$\tilde{k}_i =$	k_i	$\frac{k_i}{\sqrt{1 - \frac{C_1}{C_{pi}}}}$	$\frac{k_i}{\sqrt{1 - \frac{C_{pi}}{C_2}}}$	$\frac{k_i}{\sqrt{\left(1 - \frac{C_1}{C_{pi}}\right)\left(1 + \frac{C_1}{C_2} - \frac{C_{pi}}{C_2}\right)}}$
$C_{\text{eq}} =$	C_{pi}	$(C_{pi} - C_1)$	$\frac{C_{pi}C_2}{C_2 - C_{pi}}$	$\frac{(C_{pi} - C_1)C_2}{C_1 + C_2 - C_{pi}}$

EMS: electromechanical system; NC: negative capacitance; SP: series + parallel.

EMS with NCs. Note that equations (6) and (7) are equivalent: they both describe the EMS motion, but one is expressed as a function of \bar{V}_{sh} (i.e. equation (6)) and the other as a function of \bar{Q}_{sh} (i.e. equation (7)). ω_i^{sc} and ω_i^{oc} are the natural frequencies of the EMS when Z_{sh} is a SC ($V_{\text{sh}} = 0$) or an OC ($Q_{\text{sh}} = 0$), respectively, and their expressions are defined in Table 1. Note that their values depend on the NCs C_1 and C_2 . The term \tilde{k}_i is defined as the enhanced modal electro-mechanical coupling factor (EMEMCF) and assumes the following expression

$$\tilde{k}_i = \sqrt{\frac{(\omega_i^{\text{oc}})^2 - (\omega_i^{\text{sc}})^2}{\omega_i^2}} \quad (9)$$

Note that if we fix $\omega_i^{\text{oc}} = \hat{\omega}_i$ (where $\hat{\omega}_i$ is the OC eigenfrequency of the EMS without the addition of any NCs) and $\omega_i^{\text{sc}} = \omega_i$ (where ω_i is the SC eigenfrequency of the EMS without the addition of any NCs) in equation (9), we obtain the classical expression of the MEMCF k_i (which is close to the i th effective coupling factor; Berardengo et al., 2016b; Thomas et al., 2012)

$$k_i = \frac{\chi_i}{\omega_i \sqrt{C_{pi}}} = \sqrt{\frac{(\hat{\omega}_i)^2 - (\omega_i)^2}{\omega_i^2}} \quad (10)$$

The MEMCF measures the energy transfers between the electric circuit and the i th mode, and vice versa, through the electric network. The EMEMCF is a parameter that is analogous to the MEMCF, but it accounts for the presence of the NCs (the NCs improve the energy transfers because $\tilde{k}_i > k_i$). The analytical formulations of all the parameters involved in the definition of the EMEMCF \tilde{k}_i depend on the layout used to connect the NCs, and they are summarised in Table 1. More details on the effect of the EMEMCF can be found in Berardengo et al. (2016b).

Note that once the value of C_{pi} has been estimated and ω_i and $\hat{\omega}_i$ have been experimentally measured, the χ_i value can be derived by using equation (10).

Coupling between resonant shunt and NCs

Equations (6) to (8) describe the electrical and mechanical behaviours of the EMS when NCs are added to the EMS, and Z_{sh} is a generic passive impedance. In the case that this impedance is made from a resistance R and an inductance L , we obtain the traditional resonant shunt coupled to NCs. Note that R and L can be linked in either series or parallel (see Figure 1(d) and (e)). Therefore, six possible configurations exist (i.e. three different NC configurations and two different layouts for the connection between L and R ; see Figure 1). Equations (6) to (8) account for all the NC layouts. However, different expressions for V_{sh} and Q_{sh} must be derived according to the type of connection between R and L : series or parallel.

In the case of a parallel link between R and L , the following relation in the frequency domain links the voltage V_{sh} and the charge Q_{sh} at the impedance terminals

$$V_{\text{sh}} = -\frac{LRj\Omega}{Lj\Omega + R}j\Omega Q_{\text{sh}} \Rightarrow \bar{V}_{\text{sh}} = -C_{\text{eq}}\frac{LRj\Omega}{Lj\Omega + R}j\Omega \bar{Q}_{\text{sh}} \quad (11)$$

where j is the imaginary unit and Ω is the angular frequency. Using equation (11) together with equations (6) to (8), the following frequency response function (FRF) between q_i and F_i can be defined

$$H_i^{\text{par}}(\Omega) = \frac{q_i}{F_i} = \left(-\Omega^2 + \omega_e^2 + 2j\xi_e\omega_e\Omega \right) \cdot \left\{ \Omega^4 - \Omega^2(\omega_e^2 + 4\xi_e\xi_i\omega_i\omega_e + (\omega_i^{\text{oc}})^2) + (\omega_i^{\text{sc}})^2\omega_e^2 + j\Omega \left[2\xi_e\omega_e((\omega_i^{\text{sc}})^2 - \Omega^2) + 2\xi_i\omega_i(\omega_e^2 - \Omega^2) \right] \right\}^{-1} \quad (12)$$

Table 2. Definitions of ω_e and ξ_e for the two possible connection types of L and R .

	L and R connected in series	L and R connected in parallel
$\omega_e =$	$\sqrt{\frac{1}{LC_{eq}}}$	$\sqrt{\frac{1}{LC_{eq}}}$
$\xi_e =$	$\frac{R}{2} \sqrt{\frac{C_{eq}}{L}}$	$\frac{1}{2R} \sqrt{\frac{L}{C_{eq}}}$

Conversely, in the case of a series connection between R and L , the following relation holds

$$V_{sh} = -(Lj\Omega + R)j\Omega Q_{sh} \Rightarrow \bar{V}_{sh} = -C_{eq}(Lj\Omega + R)j\Omega \bar{Q}_{sh} \quad (13)$$

which leads to the following FRF

$$H_i^{ser}(\Omega) = \frac{q_i}{F_i} = (-\Omega^2 + \omega_e^2 + 2j\xi_e\omega_e\Omega) \cdot \left\{ \Omega^4 - \Omega^2 \left(\omega_e^2 + 4\xi_i\xi_e\omega_i\omega_e + (\omega_i^{oc})^2 \right) + (\omega_i^{sc})^2 \omega_e^2 + j\Omega [2\xi_e\omega_e((\omega_i^{oc})^2 - \Omega^2) + 2\xi_i\omega_i(\omega_e^2 - \Omega^2)] \right\}^{-1} \quad (14)$$

In the above equations, ω_e and ξ_e are the resonant frequency and the non-dimensional damping ratio of the electrical circuit, respectively, and their analytical expressions are defined in Table 2 for the two possible connection types of R and L . Note that equations (12) and (14) are valid for all the possible connections of the NC (i.e. parallel, series and SP; see Figure 1). Furthermore, they are also able to describe the behaviour of the pure resonant shunts (i.e. without NCs) if the proper values of the EMS parameters are used: $\omega_i^{sc} = \omega_i$, $\omega_i^{oc} = \hat{\omega}_i$ and $C_{eq} = C_{pi}$ (see Table 1).

If the FRF H_i (see equations 12 and 14) is multiplied by $\Phi_i(x_f)\Phi_i(x_m)$, where x_f is the point where the external force F_{ext} is applied and x_m is the point where the structural response is measured, then the FRF between the displacement and the force $U(x_m)/F_{ext}$ is found.

Stability and performance

The FRFs between a generic force F_{ext} and the structural displacement U have been derived in the previous section for all the possible configurations of NCs and R and L connections. These expressions, shown in equations (12) and (14), are the basis that allows studying the EMS stability and finding the optimal values of the electrical components of the shunt impedance and the associated attenuation performance. All these topics are addressed in the next subsections.

Stability

When an NC is used in the shunt circuit, the stability of the EMS must be verified. Indeed, the addition of NCs can cause instability due to the active nature of these components.

The stability of the EMS can be studied by applying the Routh–Hurwitz criterion (Gopal, 2002) to the FRFs of equations (12) and (14) considering both series and parallel NC layouts. The shunt circuit should always be taken into account in the analysis because it can change the stability conditions (see, as an example, the stability limits found in Berardengo et al. (2016b) for the resistive shunt coupled to NCs compared to the slightly different ones derived in De Marneffe and Preumont (2008)). To derive a closed mathematical expression for the stability conditions, the structural damping was initially neglected (i.e. $\xi_i = 0$). The derived stability conditions are the same for R and L connected both in series and in parallel

$$C_1 < C_{pi} \text{ for an IC NC connected in parallel} \quad (15)$$

$$C_2 > C_{pi}(1 + k_i^2) \text{ for an IC NC connected in series} \quad (16)$$

Then, numerical simulations were performed to determine whether a non-null damping could change these conditions. The simulations revealed that the stability conditions are not affected by a non-null value of ξ_i .

The conditions of equations (15) and (16) were derived using equations (14) and (12), which describe the EMS behaviour when an SDOF approximation is taken into account. Therefore, they are related to only one mode of the EMS. Nevertheless, when stability is studied, all the modes must be taken into account to avoid spillover effects. Therefore, the stability conditions of the entire EMS must be intended as the ones related to the modes with the strictest limits. These conditions are as follows

$$C_1 < C_\infty \text{ for an IC NC connected in parallel} \quad (17)$$

$$C_2 > C_0 \text{ for an IC NC connected in series} \quad (18)$$

where C_0 is the value of the capacitance of the piezoelectric patch at the null frequency, which can also be expressed as $C_0 = C_{pi}(1 + k_i^2)$ (Berardengo et al., 2016b). Note that the condition of equation (17) is associated with the mode at the highest frequency, whereas equation (18) is related to the lowest (i.e. the first) mode.

A similar approach can be used for the SP layout and leads to the following result

$$C_1 < C_\infty \text{ and } C_2 + C_1 > C_0 \text{ for IC NCs connected in SP} \quad (19)$$

There are two conditions for the SP configuration because there are two NCs in the circuit. Notably, the

conditions of equations (17) to (19) are equal to those found in Berardengo et al. (2016b, 2017) for a resistive shunt coupled to NCs.

Optimisation

Although several studies in the literature aimed to derive rules for the resonant shunt optimisation (e.g. Hagood and Von Flotow, 1991; Soltani et al., 2017; Thomas et al., 2012; Yamada et al., 2010), few of them accounted for the presence of NCs (e.g. Neubauer et al., 2006) and the performance and robustness with this type of enhanced shunt circuit. Among these few studies, few of the possible shunt circuit layouts were considered; this also prevents a comparison among all the possible shunt layouts. In this scenario, this section aims to derive general analytical formulae for the tuning and the performance estimation of the resonant shunt coupled to NCs, starting from the general analytical model derived previously. Therefore, thanks to the common formulation for all the NC layouts (see equations (6) to (8)), the formulations derived in the following will have a general validity and can be used for any NC configuration. Moreover, because the description is based on non-dimensional parameters (i.e. k_i , \tilde{k}_i , and the β parameters introduced later in the article), the mathematical description is valid for any given engineering problem (e.g. either mono- or bi-dimensional structures and either piezoelectric benders or stacks). This allows achieving a common mathematical description that is valid for all the possible connection types of the NC with the resonant shunt.

Note that the values of the elements composing the electrical circuit must be optimised if a high control performance is required. Indeed, the resonant shunt is not robust to mistuning, and thus, a perfect tuning between the mechanical and electrical parts of the EMS is needed (Berardengo et al., 2015a, 2016a).

Optimisation of the NC. With regard to the IC NC, it is already explained in the literature (Berardengo et al., 2016b) that the closer the NC is to C_{pi} , the higher the EMEMCF is; in turn, this implies higher potential damping performance. Therefore, it follows that the NCs must be chosen to maximise the EMEMCF, even in the case where the NCs are coupled to a resonant shunt, if the target is the maximisation of the control performance. However, the stability criteria investigated previously must be fulfilled at the same time.

To better determine the NC value that allows the best possible attenuation performance while guaranteeing stability, it is convenient to define the following indices

$$\beta_1 = \frac{C_1}{C_{pi}}, \quad \beta_2 = \frac{C_{pi}}{C_2}, \quad \beta_{sp1} = \frac{C_1}{C_{pi}}, \quad \beta_{sp2} = \frac{C_{pi}}{C_1 + C_2} \quad (20)$$

The index β_1 is related to an NC in a parallel configuration, β_2 is related to an NC in series, and β_{sp1} and β_{sp2} are related to SP. With these definitions, null β values correspond to a situation where no NCs are added to the circuit ($C_1 = 0$ and $C_2 = +\infty$). If NCs are added, then the values of the β coefficients increase from 0 towards 1. The closer the NC value is to C_{pi} , the higher the EMEMCF \tilde{k}_i is (see Table 1). This in turn improves the maximum possible damping performance. However, the β coefficients cannot be increased up to 1. Indeed, β coefficients equal to 1 mean that the values of the NCs are beyond the instability condition (as shown previously in the article).

Consequently, it is easy to understand that IC NCs in series are convenient for enhancing the EMEMCF of the low-order modes because this layout allows reaching higher β values with a stable configuration compared with the parallel connection of the IC NCs. Indeed, the value of C_{pi} is closer to C_0 than to C_∞ in this case. Conversely, IC NCs in parallel enable enhancing the EMEMCF of the high-order modes because the value of C_{pi} is closer to C_∞ than to C_0 in this case. Finally, IC NCs in SP improve the damping performance of all the modes, particularly those in the middle frequency range, as explained in Berardengo et al. (2016b).

Optimisation of the inductance. The optimisation of the value of L is achieved here by using a well-known procedure already applied to tuned mass dampers, as well as to simple piezoelectric resonant shunts (e.g. Den Hartog, 1956; Hagood and Von Flotow, 1991; Snowdon, 1968; Thomas et al., 2012). This is possible because the FRFs of equations (12) and (14) have the same form as the FRFs without NCs added (as previously shown in the article).

If we initially consider an EMS with $\xi_i = 0$, for a given value of ω_e , there exist two points F^- and F^+ at ω_F^- and ω_F^+ , respectively, which are common to all the curves $|H_i(\Omega)|$ when ξ_e is varied (see Figure 3(a)). The optimal value of ω_e (named ω_e^{opt}) is the value that makes $|H_i(\omega_F^-)| = |H_i(\omega_F^+)|$

$$\omega_e^{\text{opt}} = \omega_i^{\text{oc}} \text{ for } R \text{ and } L \text{ connected in series} \quad (21)$$

$$\omega_e^{\text{opt}} = \sqrt{\frac{3(\omega_i^{\text{sc}})^2 - (\omega_i^{\text{oc}})^2}{2}} \text{ for } R \text{ and } L \text{ connected in parallel} \quad (22)$$

Then, using the expressions in Table 2, the corresponding optimal value of the inductance, L^{opt} , can also be found.

Optimisation of the resistance. The optimal choice for ξ_e would be to make both the points F^- and F^+ maxima of $|H_i(\Omega)|$. Actually, this is not possible (Thomas et al., 2012). However, there exist two values of ξ_e , denoted

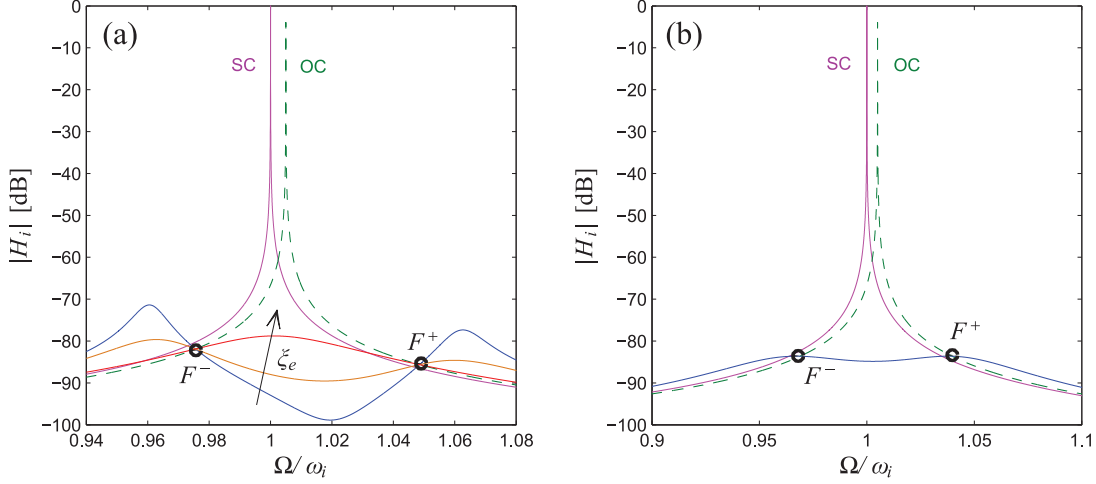


Figure 3. (a) $|H_i|$ for SC, OC and three different ξ_e values with $\omega_e > \omega_e^{\text{opt}}$ and (b) $|H_i|$ for SC, OC and with the optimal ξ_e and ω_e values (i.e. $\xi_e = \xi_e^{\text{opt}}$ and $\omega_e = \omega_e^{\text{opt}}$). $\xi_i = 0$, $k_i = 0.1$, and $C_{pi} = 40$ nF in both plots.

Table 3. Expressions of ω_{F^-} and ω_{F^+} .

Connection type	ω_{F^-}	ω_{F^+}
L and R in series	$\sqrt{(\omega_i^{\text{oc}})^2 - \omega_i^{\text{oc}} \sqrt{\frac{(\omega_i^{\text{oc}})^2 - (\omega_i^{\text{sc}})^2}{2}}}$	$\sqrt{(\omega_i^{\text{oc}})^2 + \omega_i^{\text{oc}} \sqrt{\frac{(\omega_i^{\text{oc}})^2 - (\omega_i^{\text{sc}})^2}{2}}}$
L and R in parallel	$\sqrt{(\omega_i^{\text{sc}})^2 - \omega_i^{\text{sc}} \sqrt{\frac{(\omega_i^{\text{oc}})^2 - (\omega_i^{\text{sc}})^2}{2}}}$	$\sqrt{(\omega_i^{\text{sc}})^2 + \omega_i^{\text{sc}} \sqrt{\frac{(\omega_i^{\text{oc}})^2 - (\omega_i^{\text{sc}})^2}{2}}}$

ξ_e^- and ξ_e^+ , such that one of the two aforementioned points is a maximum of the FRF amplitude (i.e. the derivative of $|H_i(\Omega)|$ with respect to Ω is set to zero at ω_{F^-} and ω_{F^+}). The optimal value of ξ_e (named ξ_e^{opt}) is chosen as the geometric mean of ξ_e^- and ξ_e^+ (i.e. $(\xi_e^{\text{opt}})^2 = ((\xi_e^-)^2 + (\xi_e^+)^2)/2$), and it results in the following

$$\xi_e^{\text{opt}} = \frac{\sqrt{3}}{2} \sqrt{\frac{(\omega_i^{\text{oc}})^2 - (\omega_i^{\text{sc}})^2}{(\omega_i^{\text{oc}})^2 + (\omega_i^{\text{sc}})^2}} \quad \text{for } R \text{ and } L \text{ connected in series} \quad (23)$$

$$\xi_e^{\text{opt}} = \frac{\sqrt{3}}{2} \sqrt{\frac{(\omega_i^{\text{oc}})^2 - (\omega_i^{\text{sc}})^2}{3(\omega_i^{\text{sc}})^2 - (\omega_i^{\text{oc}})^2}} \quad \text{for } R \text{ and } L \text{ connected in parallel} \quad (24)$$

Then, using the expressions presented in Table 2, the corresponding value of the optimal resistance R^{opt} can also be found. The FRF amplitude with ω_e^{opt} and ξ_e^{opt} is provided in Figure 3(b).

A remarkable result of equations (21) to (24) is that a common mathematical description can be found for all the possible NC layouts. Moreover, these mathematical expressions are valid even in the case of a simple resonant shunt without NCs. Indeed, equations (21) to (24) when no NCs are used in the shunt circuit are in

agreement with the formulations proposed by Yamada et al. (2010) for the pure resonant shunt without NCs. Notice that if mobility or accelerance is taken into account in place of the dynamic compliance, the optimisation formulae are slightly different (Andreaus and Porfiri, 2007; Yamada et al., 2010).

The detailed procedure used to find ξ_e^{opt} can be found in Liu and Liu (2005) and Thomas et al. (2012). Moreover, Table 3 presents the values of ω_{F^-} and ω_{F^+} for the different possible cases.

Attenuation performance

To have an estimation of the achievable attenuation, the vibration reduction provided by the resonant shunt coupled to NCs is approximated here using the attenuation index A_{dB} defined as follows

$$A_{\text{dB}} = 20 \log_{10} \frac{H_{\text{sc}}}{H_{\text{shunt}}} \quad (25)$$

where H_{sc} is the peak of $|H_i(\Omega)|$ in SC without any NC and H_{shunt} is the amplitude of $H_i(\Omega)$ at ω_{F^-} (Thomas et al., 2012) with the optimally tuned resonant shunt coupled to NCs. Recall that $H_{\text{sc}} = 1/(2\omega_i^2 \xi_i \sqrt{1 - \xi_i^2})$. Furthermore, note that $|H_i(\Omega)|$ at ω_{F^-} in the tuned condition is a good approximation of the peak of $|H_i(\Omega)|$

due to the flat shape of the FRF amplitude (see Figure 3(b)). The resulting expression of A_{dB} for R and L connected in series is presented in the following

$$A_{dB} = 10 \log_{10} \frac{S_1 + N_1}{4\omega_i^4 \xi_i^2 (1 - \xi_i^2) \left[\left((\omega_e^{\text{opt}})^2 - \omega_{F-}^2 \right)^2 + (2\omega_e^{\text{opt}} \xi_e^{\text{opt}} \omega_{F-})^2 \right]} \quad (26)$$

while the expression of A_{dB} for R and L connected in parallel is as follows

$$A_{dB} = 10 \log_{10} \frac{P_1 + N_1}{4\omega_i^4 \xi_i^2 (1 - \xi_i^2) \left[\left((\omega_e^{\text{opt}})^2 - \omega_{F-}^2 \right)^2 + (2\omega_e^{\text{opt}} \xi_e^{\text{opt}} \omega_{F-})^2 \right]} \quad (27)$$

where

$$S_1 = \left[2\omega_i \xi_i \left((\omega_e^{\text{opt}})^2 - \omega_{F-}^2 \right) + 2\omega_e^{\text{opt}} \xi_e^{\text{opt}} \left((\omega_i^{\text{oc}})^2 - \omega_{F-}^2 \right) \right]^2 \omega_{F-}^2 \quad (28)$$

$$N_1 = \left[\omega_{F-}^4 + (\omega_e^{\text{opt}})^2 (\omega_i^{\text{sc}})^2 - \left((\omega_i^{\text{oc}})^2 + (\omega_e^{\text{opt}})^2 + 4\omega_i \omega_e^{\text{opt}} \xi_i \xi_e^{\text{opt}} \right) \omega_{F-}^2 \right]^2 \quad (29)$$

$$P_1 = \left[2\omega_i \xi_i \left((\omega_e^{\text{opt}})^2 - \omega_{F-}^2 \right) + 2\omega_e^{\text{opt}} \xi_e^{\text{opt}} \left((\omega_i^{\text{sc}})^2 - \omega_{F-}^2 \right) \right]^2 \omega_{F-}^2 \quad (30)$$

The expressions of equations (27) and (26) can be rearranged using the expressions of Table 1 to obtain the expression of A_{dB} as a function of ξ_i , k_i and \tilde{k}_i . These expressions are provided in Appendix 2. Note that the expression of the attenuation depends only on ξ_i and \tilde{k}_i when an NC in parallel is used. Conversely, when a series NC is taken into account, k_i also appears in the expressions of the attenuation. For the SP, the attenuation expressions depend on ξ_i and \tilde{k}_i and k_i and β_{sp1} . This means that different values of the attenuation are expected for different NC layouts once the values of ξ_i and \tilde{k}_i are fixed.

Figure 4 shows the performance of the different shunt configurations for three different ξ_i values for an NC in either series or parallel and the two possible connections of R and L . Henceforth, we will add two superscripts to the symbol A_{dB} to specify the shunt layout that the attenuation refers to. The first superscript indicates the connection between R and L (S = series and P = parallel), while the second superscript indicates the NC layout (S = series, P = parallel, and SP = series + parallel). For example, $A_{dB}^{P,SP}$ is the attenuation for R and L in parallel and NC in the SP configuration;

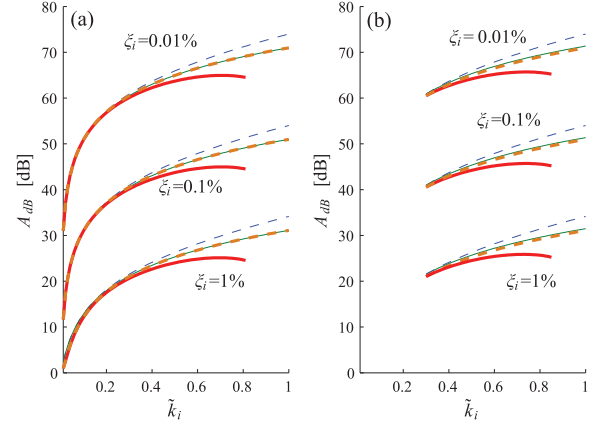


Figure 4. A_{dB} trend as a function of \tilde{k}_i for different ξ_i values: (a) $k_i = 0.01$ and (b) $k_i = 0.3$. Solid thick red line for $A_{dB}^{P,P}$, dashed thick orange line for $A_{dB}^{P,S}$, dashed thin blue line for $A_{dB}^{S,P}$ and solid thin green line for $A_{dB}^{S,S}$. The lines related to $A_{dB}^{P,P}$ and $A_{dB}^{S,S}$ are always almost superimposed.

$A_{dB}^{S,P}$ is the attenuation for R and L in series and NC in the parallel configuration. Note that Figure 4 also allows comparing the damping performance of the pure resonant shunt (i.e. with no NCs added) and that of the resonant shunt coupled to NCs. Indeed, the first point (on the left) of each curve of the plot shows the attenuation provided by the pure resonant shunt (i.e. $\tilde{k}_i = k_i$), while all the other points of the same curve describe the attenuation as a function of the EMEMCF \tilde{k}_i , which is increased from the value of k_i by adding NCs in the electrical circuit. Such a comparison will also be possible for the other plots of the same type presented later in this article.

Figure 4 shows that the NC in the parallel configuration provides better attenuation compared to the NC in series with the same value of \tilde{k}_i . Furthermore, the connection of R and L in series is able to enhance the attenuation more than the connection in parallel.

Notably, for R and L in parallel and NC in series, the curves of Figure 4 stop for \tilde{k}_i close to 0.8. This result occurs because the optimisation criterion of equations (22) and (24) cannot be applied for higher \tilde{k}_i values because the quantity $[3(\omega_i^{\text{sc}})^2 - (\omega_i^{\text{oc}})^2]$ becomes lower than zero. From a physical perspective, this situation is related to the case in which the value of ω_{F-}^2 becomes negative (see Table 3). As mentioned, this occurs when \tilde{k}_i is increased over a certain value, and this threshold value depends on the value of k_i . A similar result occurs even for NC in parallel and L and R connected in parallel but for values of \tilde{k}_i much higher than 0.8 (i.e. for $\tilde{k}_i > \sqrt{2}$, thus not interesting in practical applications). This topic will be treated in more detail later in this section.

For the NC SP layout (see Figure 5), the curve of A_{dB} has the same shape as the curve related to the NC in series, but the attenuation performance is between that of the NC in parallel and that of the NC in series.

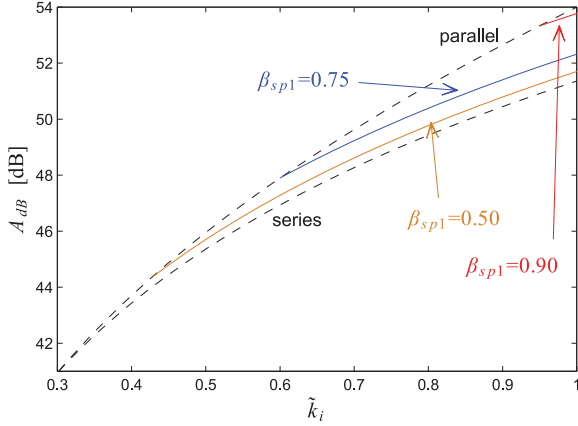


Figure 5. A_{dB} trend as a function of \tilde{k}_i for different NC layouts: $\xi_i = 0.1\%$ and $k_i = 0.3$. Dashed lines for NC in series and parallel, and solid lines for NCs in SP with different values of β_{sp1} . R and L are connected in series.

When the value β_{sp1} is increased (i.e. the parallel NC is pushed towards the stability limit), the SP curve shifts upwards and tends to the parallel NC curve. Conversely, if β_{sp1} is close to 0, the SP tends to behave as the series. As in the previous cases, also for NCs in the SP configuration, a series connection between R and L provides attenuation levels that are some decibels higher than in the case of R and L connected in parallel. Furthermore, as in the case of the NC in series, also in the case of NCs in SP, a parallel connection between L and R prevents reaching high \tilde{k}_i values because ω_{F-}^2 becomes negative. The value at which this situation occurs depends on the values of k_i and β_{sp1} . A more detailed analysis of the NC SP layout will be provided in the next subsection.

The attenuation provided by different NC layouts is thus different for high \tilde{k}_i values (see Figures 4 and 5). This is in contrast to what occurs for a resistive shunt coupled to NCs (Berardengo et al., 2016b). Indeed, in the latter case, although the expressions of A_{dB} are different, the differences in terms of attenuation level achieved for different NC layouts are so small that they can be neglected.

The previous analysis has been performed using optimisation criteria that neglect the structural damping. With non-zero structural damping, the gain curves no longer cross at points F^+ and F^- , although they remain very close to this condition if ξ_i is small enough. Therefore, we also computed the actual maxima of $|H_i(\Omega)|$ and no longer in ω_{F-} . These actual maxima, $A_{dB,num}$, have been computed by calculating the value of $|H_i(\Omega)|$ frequency by frequency for the different shunt configurations.

First, the connection between R and L in series is taken into account. The case of R and L in parallel will be addressed later in this section. Figure 6 shows the $A_{dB,num}$ results for R and L in series for some NC layouts (i.e. parallel and series; SP is not shown because it

has a similar behaviour) compared to the A_{dB} values. It is evident that the values of the index A_{dB} are accurate estimations of the actual attenuation values, with an exception for the case of series (and SP) NCs at very high values of \tilde{k}_i . Hence, a specific discussion is needed for the behaviour of $A_{dB,num}$ at high \tilde{k}_i values for an NC connected in series (or NCs in SP).

The series and SP NC layouts make the SC eigenfrequency shift towards increasingly lower frequency values (Berardengo et al., 2016b, 2017; De Marneffe and Preumont, 2008). When such a shift is high (i.e. with high β_2 or β_{sp2} values and thus high values of \tilde{k}_i), the gain of H_i at low frequency increases considerably (see Figure 7). This has two different consequences, depending on the connection of R and L . For R and L in series, the point F^- becomes a relative minimum (see Figure 7) rather than a maximum. Hence, the value of $|H_i|$ at frequencies lower than ω_{F-} becomes higher than $|H_i(\omega_{F-})|$ and $|H_i(\omega_{F+})|$. However, this increase in the FRF gain is at low-frequency values that are far from ω_i and thus could be not critical for many specific applications. For R and L in parallel, the value of ω_{F-}^2 becomes negative, thus preventing the use of the shunt optimisation criteria for L and R found previously, as already observed. However, the values of \tilde{k}_i for which the aforementioned effects appear are quite high (approximately 0.8). Such high values of \tilde{k}_i are difficult to achieve in practical applications, and thus, the highlighted issues can be neglected in many practical applications.

Note that the attenuation provided by the index A_{dB} , evaluated considering the FRF amplitude at ω_{F-} , satisfactorily describes the actual attenuation $A_{dB,num}$ even in the case of very high \tilde{k}_i when the increase of the static stiffness is neglected (see the upper branches related to the curves of $A_{dB,num}^{S,S}$ in Figure 6). Indeed, as already mentioned, the FRF amplitude, achieved with the presented optimisation criterion, has a flat shape between ω_{F-} and ω_{F+} (see Figure 3(b)).

Regarding the connection of L and R in parallel, A_{dB} and $A_{dB,num}$ differ by less than 0.5 dB for high \tilde{k}_i values. Clearly, if we consider NCs in series (or SP), the comparison can be performed for \tilde{k}_i values up to approximately 0.8, as already explained. No figures related to such a comparison are presented here for the sake of conciseness and because they would not add to the discussion.

Figure 8 provides a comparison between the attenuations $A_{dB,num}$ achieved with the two different types of connections between R and L : between $A_{dB,num}^{S,P}$ and $A_{dB,num}^{P,P}$ and between $A_{dB,num}^{S,S}$ and $A_{dB,num}^{P,S}$. It is evident that the layout with L and R in series ensures higher attenuation compared to the parallel connection. Furthermore, Figure 8 provides a clear picture of the behaviour of the different possible shunt layouts, providing a summary of the discussion to this point.

A further remarkable result is shown in Figure 9, where the dynamic magnification factor D is plotted for

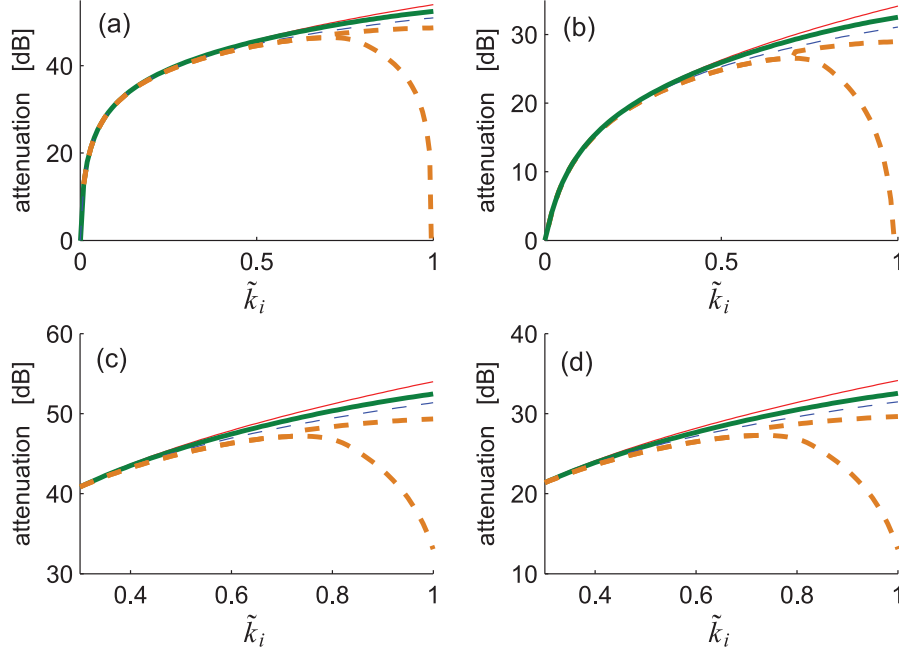


Figure 6. A_{dB} and $A_{dB,num}$ for a system with (a) $k_i = 0.01$ and $\xi_i = 0.1\%$, (b) $k_i = 0.01$ and $\xi_i = 1\%$, (c) $k_i = 0.3$ and $\xi_i = 0.1\%$ and (d) $k_i = 0.3$ and $\xi_i = 1\%$. R and L connected in series. Thin solid line for $A_{dB}^{S,P}$, thick solid line for $A_{dB,num}^{S,P}$, thin dashed line for $A_{dB}^{S,S}$ and thick dashed line for $A_{dB,num}^{S,S}$. The thick dashed line is split into two branches: the upper branch is the attenuation calculated considering the peak of the FRF amplitude at the highest frequency, thus close to F^+ (see Figure 3b), and the lower branch is the actual attenuation calculated considering the highest peak of the FRF amplitude, which takes into account the behaviour of the controlled FRF at low frequency.

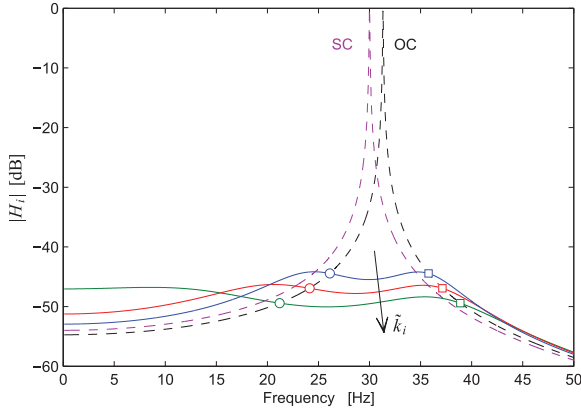


Figure 7. $|H_i|$ for a system with $k_i = 0.3$, $\xi_i = 0.1\%$, $\omega_i/(2\pi) = 30$ Hz and three different values of \tilde{k}_i : 0.45, 0.6 and 0.8. The NC is connected in series, and L and R are in series. Circles (\circ) indicate the points F^- related to the different curves, while squares (\square) indicate the points F^+ . The value of ω_{F^-} is at 21.2 Hz for the case of $\tilde{k}_i = 0.8$; it is not exactly a minimum because ξ_i^{opt} is used in place of ξ_i^- .

different NC configurations and ξ_i values. The dynamic magnification factor is defined as the ratio between H_{shunt} (see previously in this section) and H_0 , where H_0 is $|H_i(\Omega = 0)|$ in SC without NCs

$$D = \frac{H_{\text{shunt}}}{H_0} = \frac{H_{\text{shunt}}}{1/\omega_i^2} \quad (31)$$

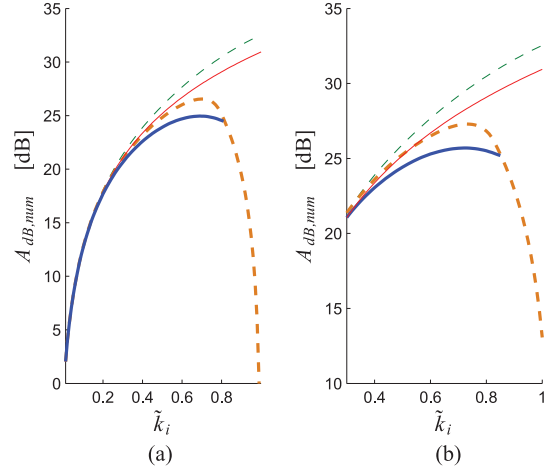


Figure 8. $A_{dB,num}$ for a system with (a) $k_i = 0.01$ and $\xi_i = 1\%$ and (b) $k_i = 0.3$ and $\xi_i = 1\%$. Thin solid line for $A_{dB,num}^{P,P}$, thin dashed line for $A_{dB,num}^{S,P}$, thick solid line for $A_{dB,num}^{P,S}$, and thick dashed line for $A_{dB,num}^{S,S}$.

Figure 9 shows that for \tilde{k}_i values between approximately 0.1 and 0.5, all the curves tend to superimpose, regardless of the layout of NC and L and R connections as well as the value of ξ_i . The only parameter affecting D is \tilde{k}_i . When \tilde{k}_i is lower than approximately 0.1, the curves group according to the type of R and L connection and the value of ξ_i ; conversely, the type of NC has a low effect (i.e. the curves related to NCs in

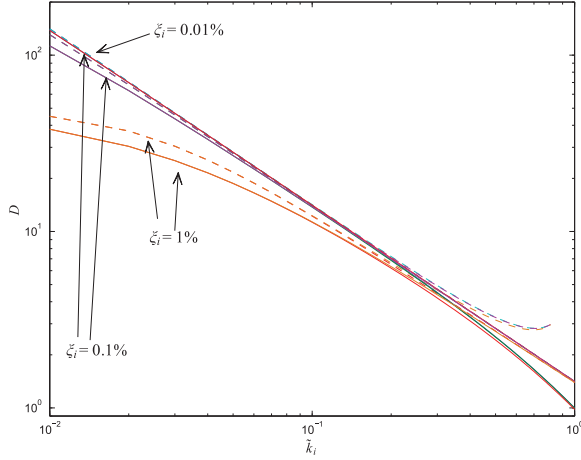


Figure 9. Trend of D for a system with $k_i = 0.01$ and different ξ_i values. Dashed lines for R and L connected in parallel, and solid lines for R and L connected in series. NCs in series and parallel.

parallel and series with the same type of L and R connection and the same damping value are almost merged in Figure 9). When \tilde{k}_i increases over approximately 0.5, the curves split according to the NC type (i.e. parallel and series) and R and L connection, while the damping value has no effect. Indeed, three groups can be distinguished here:

- The upper one composed of the curves related to NCs in series and R and L connected in parallel (which stop at \tilde{k}_i equal to approximately 0.8);
- The group in the middle is composed of the curves related to NCs in series and R and L connected in series and of the curves related to NCs in parallel and R and L connected in parallel;
- The lower one composed of the curves related to NCs in parallel and R and L connected in series.

For the SP layout, its curves are always between those of the parallel and series layouts, according to the value of β_{sp1} .

A remarkable result is that impedances composed of an NC in parallel and R and L connected in series are able to make D lower than 1 when \tilde{k}_i is close to 1. Values of D lower than 1 mean that the height of the FRF peak becomes smaller than the static FRF amplitude.

Figures 7 and 9 show that the use of the classical resonant shunt together with the use of NCs can lead to the cancellation of resonance peaks. This is a remarkable result that reveals the high damping performance provided by this control approach.

This section (together with the following one) has allowed providing a complete comparison of the various connection layouts, together with evidence that the considered type of vibration damping allows achieving resonance cancellation, which is a remarkable result.

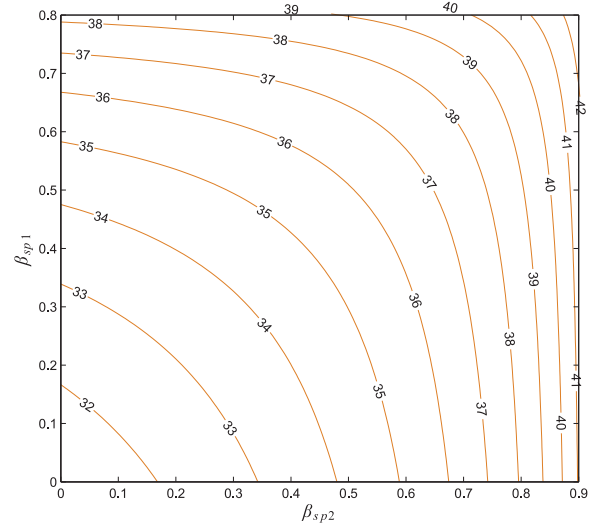


Figure 10. $A_{dB}^{S,SP}$ for a system with $k_i = 0.1$ and $\xi_i = 0.1\%$. The system is supposed to become unstable for $\beta_1 > 0.8$ and $\beta_2 > 0.9$. Therefore, the β_{sp1} and β_{sp2} axes are limited to 0.8 and 0.9, respectively. The isolines represent the value of $A_{dB}^{S,SP}$ in decibels. Note that for this example, the maximum value of \tilde{k}_i that can be reached is lower than 0.4, and thus, no problems related to the increase in the gain at low frequency with the SP and series NCs occur.

Advantages of the SP layout

A remarkable benefit provided by the NC in the SP layout is that it can offer the same attenuation provided by NCs in either a parallel or series layout but staying further from the stability limits (i.e. lower β values). This is demonstrated by Figure 10, which shows the β_{sp1} and β_{sp2} values that must be chosen for the SP configuration to reach a given attenuation value for the system chosen as an example. Figure 10 also shows the attenuation for an NC in series (see the horizontal axis of Figure 10 where $\beta_{sp1} = 0$) and an NC in parallel (see the vertical axis of the figure where $\beta_{sp2} = 0$). It is evident that the SP allows reaching the same attenuation (see the iso-attenuation lines in Figure 10) of the NC in either series or parallel with lower β values, which means having a safer margin from the unstable condition. Moreover, note that the use of β_{sp1} and β_{sp2} values equal to β_1 and β_2 , respectively, leads to higher attenuation levels for the SP compared to the NC in either parallel or series, which is a further advantage of the SP layout.

Robustness of the vibration control

This section discusses the effect of mistuning on the values of ω_e and ξ_e . This is an important analysis because the shunt system can often find itself working in mistuned conditions in practical applications. Indeed, the system can undergo changes in its characteristics over time. For example, a mistuning can easily be caused by a thermal shift, which can cause changes in the

electrical parameters of the shunt circuit and in the natural frequency of the system. Moreover, a mistuning can be experienced even in the case of high uncertainty associated with the values of the different system parameters. Therefore, it may be useful for the user to have an estimation of the performance loss in the case of a non-perfect tuning of the considered system to choose the best NC and R and L connection configuration. The aim of the authors in this section is not to provide methods for predicting the loss of performance when the shunt finds itself working in mistuned conditions. Indeed, this analysis is already available in the literature (Andreaus and Porfiri, 2007; Berardengo et al., 2015a, 2016a) for the resonant shunt without NCs (and it can be extended to the case in which NCs are coupled to the resonant shunt considering that the addition of an NC, either in series or in parallel, aims at increasing the achievable attenuation acting on the system coupling coefficient). Nevertheless, a comparison in terms of robustness (where the term robustness indicates the capability of limiting the performance loss due to mistuning) between the two different connection types of R and L and among the three different NC layouts is missing in the literature. In light of this, this section aims to highlight any different behaviour in terms of robustness among different shunt configurations to determine whether there is one layout that is more robust to mistuning than the others.

In this analysis, the mistuned values of ω_e and ξ_e will be indicated by means of an asterisk as ω_e^* and ξ_e^* . The corresponding attenuation will be indicated as $A_{dB,num}^{*,S,P}$. Figure 11 shows the trend of $A_{dB,num}^{*,S,P}$, and it confirms that the resonant shunt suffers significant performance losses when working in mistuned conditions, even when adding NCs. Therefore, it is important to compare different shunt layouts in terms of robustness to determine whether there is a circuit configuration that behaves better than the others.

Figure 12 compares the different NC layouts; it presents some examples of the difference between the attenuation in mistuned conditions provided by IC NCs in series and in parallel configurations keeping the same R and L connection (i.e. plots (a) and (b) for R and L in series and plots (c) and (d) for R and L in parallel). It is evident that the NC in series offers almost the same attenuation compared to the NC in parallel when a mistuned condition is considered.

Figure 13 compares the effect on the robustness of the type of connection between R and L while keeping the same NC layout. Figure 13 shows the difference between the attenuation in mistuned conditions provided by R and L connections in series and parallel for an IC NC in parallel in plots (a) and (b) and in series in plots (c) and (d). It is evident that the parallel connection between R and L becomes highly advantageous when $\omega_e^* \ll \omega_e^{opt}$. In the other cases, the series connection between R and L remains the best one.

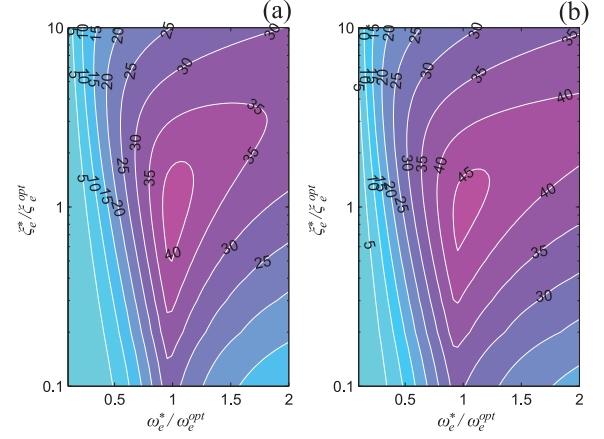


Figure 11. $A_{dB,num}^{*,S,P}$ for a system with $\xi_i = 0.1\%$ and $k_i = 0.2$: (a) $k_i = 0.4$ and (b) $k_i = 0.6$.

All the discussions presented thus far are related to IC NCs. The next section discusses the adoption of RC NCs. Therefore, the effects of the use of RC NCs on stability, tuning and performance will be addressed.

The effects of the NC implementation on system stability and damping performance

As mentioned in the introduction, in some cases, RCs must be used in place of ICs because of their higher reliability. The aim of this section is not to explain how to build RCs but rather to illustrate the effects of RCs coupled to a resonant shunt on the damping performance and stability of the EMS. Indeed, there are many differences in terms of EMS behaviour compared to the case of using ICs, and this point is often neglected in the literature, even if it is important to consider it to ensure an effective damping action. To this end, a brief introduction about how to construct RCs is presented herein to make the overall discussion clear.

The IC NCs can be practically built using an OP-AMP. Among the different possible circuit layouts available in the literature (Berardengo et al., 2016b), we consider only two of them here, as shown in Figure 14(a) and (b). These two circuits can be viewed as pure NCs, where the global NC at the circuit terminals, generically called $-\tilde{C}$ here, can be calculated solving the circuits (Berardengo et al., 2016b; De Marneffe and Preumont, 2008)

$$\tilde{C} = \frac{R_2}{R_1} \hat{C} \quad (32)$$

When NCs in series (as well as the series part of the SP) are considered, an additional resistance \hat{R} is often needed (see Figure 14(c)) to solve problems such as bias currents, which prevent the correct functioning of the circuit (Moheimani and Fleming, 2006). This additional element makes the circuit no longer behave as a pure

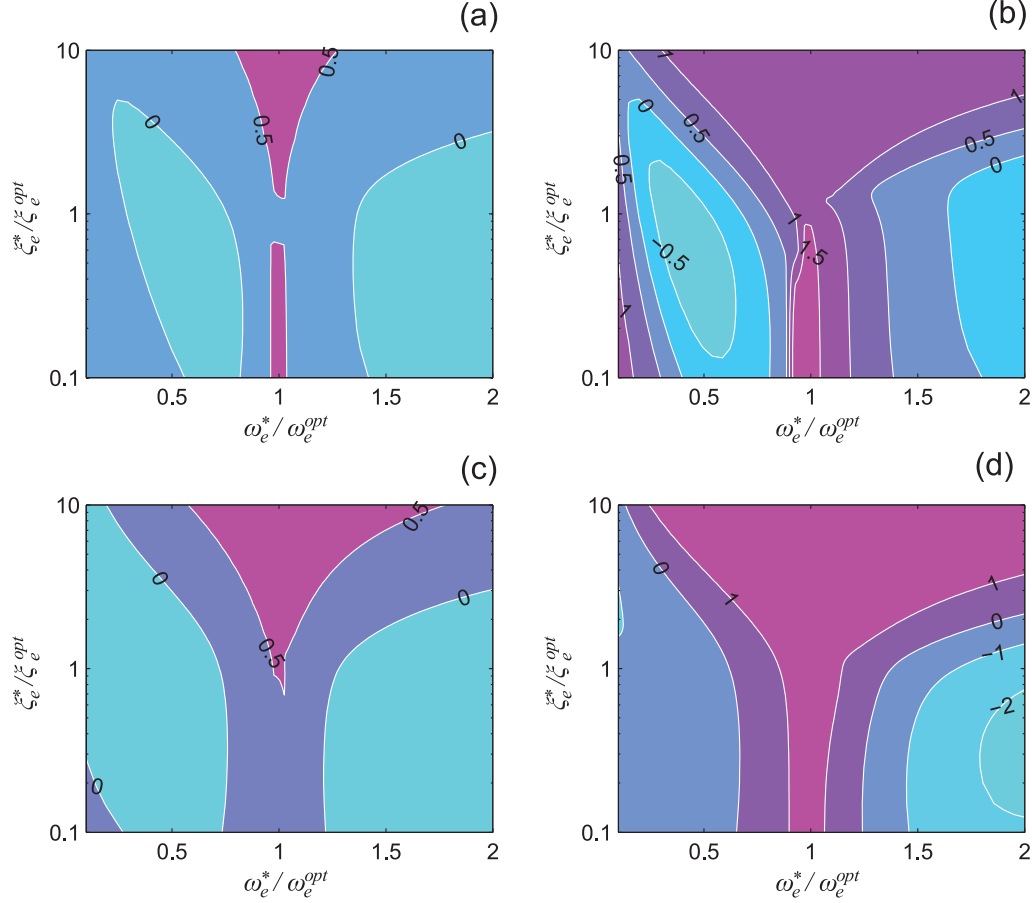


Figure 12. $A_{\text{dB,num}}^{*,S,P} - A_{\text{dB,num}}^{*,S,S}$ for a system with $\xi_i = 0.1\%$ and $k_i = 0.2$: (a) $\tilde{k}_i = 0.4$ and (b) $\tilde{k}_i = 0.6$. $A_{\text{dB,num}}^{*,P,P} - A_{\text{dB,num}}^{*,P,S}$ for a system with $\xi_i = 0.1\%$ and $k_i = 0.2$: (c) $\tilde{k}_i = 0.4$ and (d) $\tilde{k}_i = 0.6$.

NC but rather as the parallel of an NC, $-\tilde{C}$ (see equation (32)), and a negative resistance $-\tilde{R}$ (Berardengo et al., 2016b)

$$\tilde{R} = \frac{R_1}{R_2} \hat{R} \quad (33)$$

The effect of $-\tilde{R}$ is to make the OP-AMP circuit behave differently from a pure NC at low frequency (Berardengo et al., 2016b). This in turn causes a worsening of the attenuation performance when low-frequency modes are involved (Berardengo et al., 2016b) and has a destabilising effect (Berardengo et al., 2016b; Manzoni et al., 2012). Berardengo et al. (2016b) suggested the addition of a compensation resistance R_s in parallel to $-\tilde{R}$ (see Figure 14(d)). This can cause an offset on the OP-AMP output voltage but improves the control performance and makes the circuit more robust to instability. The model of the electrical circuit with the addition of R_s is the parallel between $-\tilde{C}$ and a resistance R_{eq} (Berardengo et al., 2016b), with

$$R_{\text{eq}} = \frac{R_s \tilde{R}}{\tilde{R} - R_s} \quad (34)$$

R_s is chosen to make R_{eq} as close as possible to $-\infty$, which is a situation similar to an IC NC. When an NC with the addition of \tilde{R} and the absence of the compensation resistance of R_s is used, it cannot be considered as a pure NC. We refer to these circuits as RC NCs. Conversely, the use of R_s , with values such that R_{eq} tends to $-\infty$, makes an RC NC behave as an IC NC.

This section analyses the effect of the value of R_{eq} on the behaviour of the shunt damping. Specifically, the next subsection analyses the attenuation performance of the RC NC, while the subsequent subsection addresses the stability of the EMS. Since the series connection between R and L provides better attenuation performance than the parallel link (see the previous discussion in the article), we will refer to the series connection henceforth. Note that the use of electrical schemes different from those of Figure 14 to implement the NCs would lead to the same models of IC NCs and RC NCs and to the same results discussed in this section (Berardengo et al., 2016b).

Performance analysis

As mentioned previously, IC NC circuits and RC NC circuits exhibit different behaviour in the low-frequency

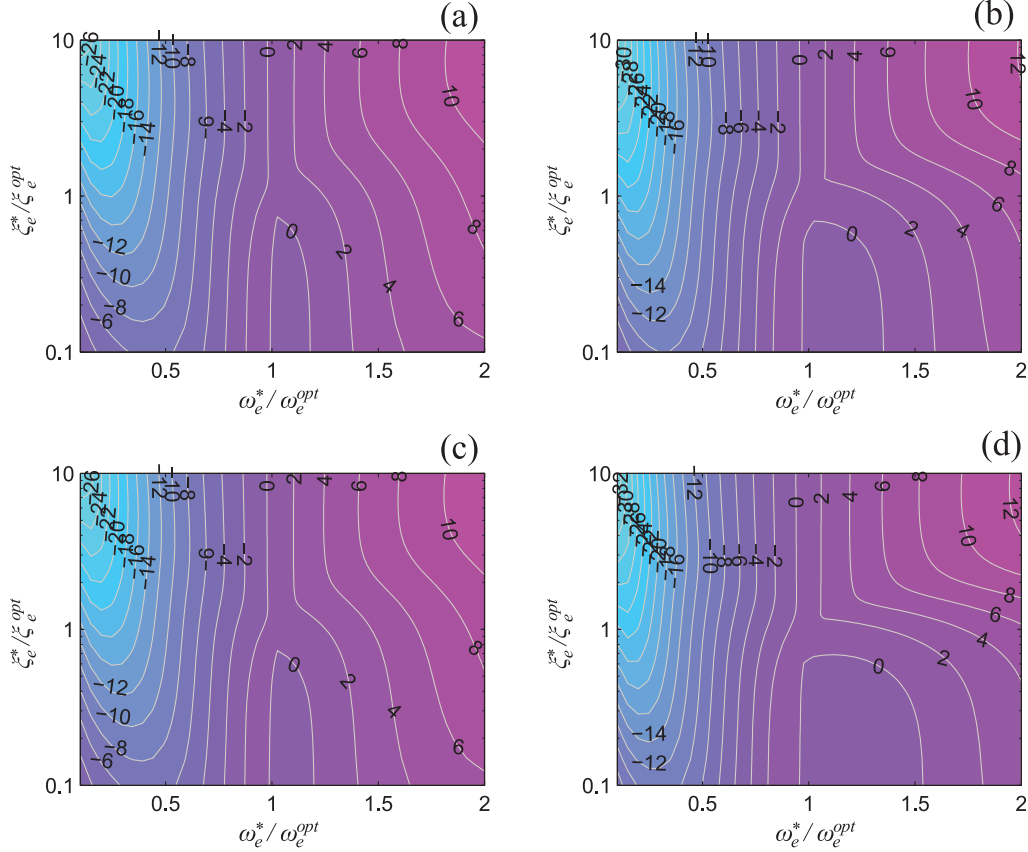


Figure 13. $A_{dB,num}^{*,S,P} - A_{dB,num}^{*,P,P}$ for a system with $\xi_i = 0.1 \%$ and $k_i = 0.2$: (a) $\tilde{k}_i = 0.4$ and (b) $\tilde{k}_i = 0.6$. $A_{dB,num}^{*,S,S} - A_{dB,num}^{*,P,S}$ for a system with $\xi_i = 0.1 \%$ and $k_i = 0.2$: (c) $\tilde{k}_i = 0.4$ and (d) $\tilde{k}_i = 0.6$.

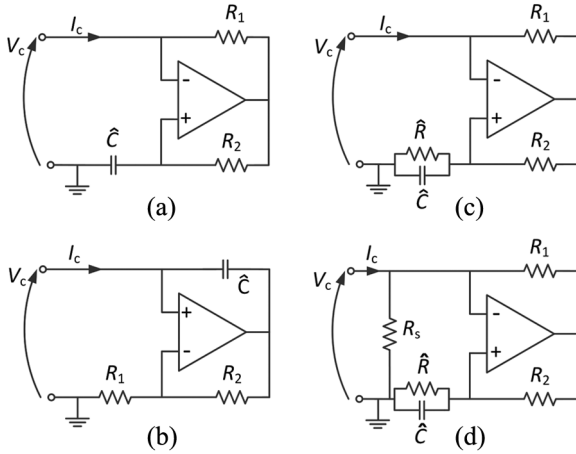


Figure 14. Practical implementation of NCs: (a) IC NC for connection in series (as well as for the series part of SP), (b) IC NC for connection in parallel (as well as for the parallel part of SP), (c) RC NC for connection in series (as well as for the series part of SP) and (d) the use of the compensation resistance in RC NC for connection in series (as well as for the series part of SP).

range. When R_s is used, the behaviour of the RC NC electrical network tends to that of the IC NC, depending on the value of R_s used. This is clearly shown in

Figure 15. Figure 15 compares the impedance Z_{imp} of different circuits: a circuit made from the series of L , R and an IC NC and circuits made from the series of L , R and an RC NC with different levels of compensation (i.e. different values of R_{eq}). It is evident that their behaviours at low frequency are different. This in turn means that the behaviour of the shunted EMS will be different from the expected behaviour when an RC NC is used in place of an IC NC.

Using an approach similar to that employed for IC NCs, it is possible to find the SDOF FRF, H_i^{real} , for an RC NC in series and L and R connected in series (the same approach can easily lead to the expression of the FRF for L and R connected in parallel)

$$H_i^{real} = \frac{q_i}{F_i} = \frac{-B_3 j \Omega^3 - B_2 \Omega^2 + B_1 j \Omega + 1}{A_5 j \Omega^5 + A_4 \Omega^4 - A_3 j \Omega^3 - A_2 \Omega^2 + A_1 j \Omega + \omega_i^2} \quad (35)$$

where

$$A_5 = C_{pi} L \tilde{R} \tilde{C} \quad (36)$$

$$A_4 = C_{pi} (L + R \tilde{R} \tilde{C} + 2 \xi_i \omega_i L \tilde{R} \tilde{C}) \quad (37)$$

$$A_3 = \tilde{R} \tilde{C} + C_{pi} [R - \tilde{R} + L \tilde{R} \tilde{C} \hat{\omega}_i^2 + 2 \xi_i \omega_i (L + R \tilde{R} \tilde{C})] \quad (38)$$

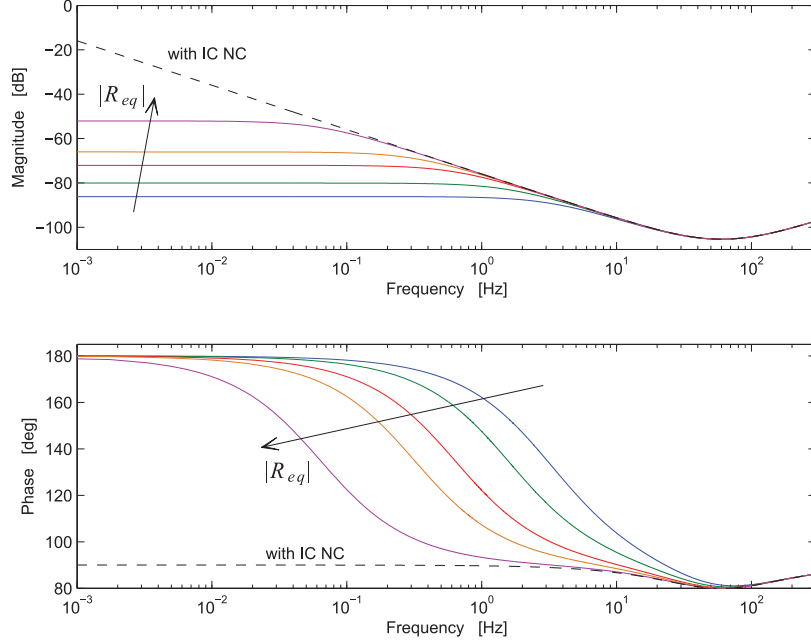


Figure 15. Magnitude and phase of the impedance Z_{imp} for different values of R_{eq} . In this figure, $L = 140.72$ H, $R = 18.89$ k Ω , $\tilde{C} = 50$ nF and $R_{\text{eq}} = -\infty, -50, -10, -5, -2, -1$ M Ω . The case with $R_{\text{eq}} = -\infty$ corresponds to the case of using an IC NC (dashed line).

$$A_2 = 1 + 2\xi_i\omega_i[\tilde{R}\tilde{C} + C_{\text{pi}}(R - \tilde{R})] + \hat{\omega}_i^2 C_{\text{pi}}(L + R\tilde{R}\tilde{C}) \quad (39)$$

$$A_1 = 2\xi_i\omega_i + \hat{\omega}_i^2[\tilde{R}\tilde{C} + C_{\text{pi}}(R - \tilde{R})] - \tilde{R}\tilde{C}\omega_i^2 k_i^2 \quad (40)$$

and

$$B_3 = C_{\text{pi}}L\tilde{R}\tilde{C} \quad (41)$$

$$B_2 = C_{\text{pi}}(L + R\tilde{R}\tilde{C}) \quad (42)$$

$$B_1 = \tilde{R}\tilde{C} + C_{\text{pi}}(R - \tilde{R}) \quad (43)$$

Then, from the FRF expression of equation (35), it is possible to derive the attenuation performance, named $A_{\text{dB, real}}$ here, that is achievable using RCNCs and employing the optimal values of R and L derived from the IC NC analysis (see equations (21) and (23)).

Figure 16 shows $A_{\text{dB, real}}$, found by calculating the maximum of $|H_i^{\text{real}}|$ employing equation (35), for an EMS used as an example with the eigenfrequency in the low-frequency range.

When R_{eq} is negative and $|R_{\text{eq}}|$ is high (e.g. $|R_{\text{eq}}| = 75$ M Ω), the RC NC behaves as an IC NC and the attenuation increases. It is easily observed that the lower the value of $|R_{\text{eq}}|$ (i.e. which corresponds to the case of poor compensation) is, the farther the attenuation is from the theoretical value of A_{dB} and the worse the attenuation is. One possibility to increase the attenuation in the presence of low values of $|R_{\text{eq}}|$ is to find new optimal values of the resistance and inductance, named $R_{\text{min}}^{\text{opt}}$ and $L_{\text{min}}^{\text{opt}}$, respectively (the consequent attenuation is named $A_{\text{dB, min}}$), as shown in

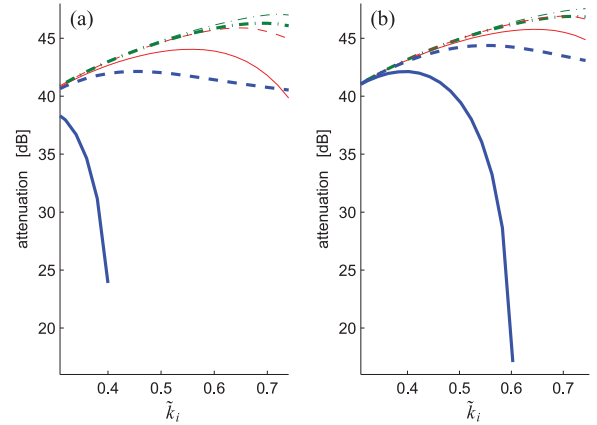


Figure 16. Trends of $A_{\text{dB, real}}$ and $A_{\text{dB, min}}$ for a system with $\omega_i/2\pi = 30.5$ Hz, $\xi_i = 0.1\%$ and $k_i = 0.2$ for an NC (a) in series and NCs (b) in SP with $\beta_{\text{sp1}} = 0.5$ for different values of R_{eq} . Solid thick line for $A_{\text{dB, real}}$ and $R_{\text{eq}} = -1$ M Ω , dashed thick line for $A_{\text{dB, min}}$ and $R_{\text{eq}} = -1$ M Ω , solid thin line for $A_{\text{dB, real}}$ and $R_{\text{eq}} = -10$ M Ω , dashed thin line for $A_{\text{dB, min}}$ and $R_{\text{eq}} = -10$ M Ω , dashed-dotted thick line for $A_{\text{dB, real}}$ and $R_{\text{eq}} = -75$ M Ω , and dashed-dotted thin line for $A_{\text{dB, min}}$ and $R_{\text{eq}} = -75$ M Ω .

Figure 16. These new optimal values can be found by numerical minimisation of the maximum of $|H_i^{\text{real}}|$ (see equation (35)). It follows that the use of proper values of the compensation resistance R_s allows employing the theoretical formulations for the optimal shunt parameters and the consequent attenuation even with RC NCs. Conversely, when R_s is not used or compensation is not proper, a numerical minimisation is needed for

finding new L and R optimal values to obtain satisfactory attenuation levels at low frequency. Another solution to improve the performance in the case of non-proper compensation (or even no use of R_s) is to employ an SP layout for the NC. Indeed, from comparing Figure 16(a) and (b), the SP is able to improve the attenuation performance of the RC NC in series even for low values of $|R_{eq}|$.

Stability analysis

The previous subsection has shown that the use of RC NCs deteriorate the attenuation at low frequency if R_s is not used. Another effect of RC NCs is related to the stability of the EMS. Indeed, Figure 16 shows that the curves of $A_{dB, real}$ related to $|R_{eq}| = 1 \text{ M}\Omega$ (blue thick solid curves in Figure 16) stop at a given low value of \tilde{k}_i . The reason for this result is that the EMS becomes unstable after that \tilde{k}_i value, even if the stability conditions for IC NCs in series or SP layout are met. Indeed, the presence of \hat{R} causes instability at low frequency and makes the stability constraint stricter compared to the use of IC NCs. Therefore, from Figure 16, it can be deduced that the use of the compensation resistance allows not only enhancing the performance but also even improving the stability conditions, making them increasingly closer to the theoretical ones valid for IC NCs. Furthermore, the comparison of Figure 16(a) and (b) also shows that the SP (compared to the series NC) is able to improve the stability even for low values of $|R_{eq}|$.

The issue related to the stability of the EMS when using RC NCs in series can be further deepened, taking into account the fact that all the modes of the EMS must be stable, not only those on which the control action is focused. Consider, as an example, an EMS with two modes at ω_1 and ω_2 , with $\omega_2 > \omega_1$. The damping action is focused on the mode at ω_2 (using R_{min}^{opt} and L_{min}^{opt}), and stability is investigated for both of the modes. The use of L_{num}^{opt} and R_{num}^{opt} is analysed here since it allows increasing the performance and the stability of the controlled mode, as shown in Figure 16. Therefore, the situation considered in the example is the most favourable from the stability perspective. The trend of the poles of the EMS is analysed to study the stability. The poles of the second mode have a negative real part for all the considered values of \tilde{k}_i (i.e. the mode is stable; this is also because the numerical minimisation used to find R_{min}^{opt} and L_{min}^{opt} imposes the stability of the mode). This does not occur for the first mode. Figure 17(a) shows that one of the poles related to the first mode has a positive real part (i.e. instability) for some \tilde{k}_2 and R_{eq} values. Particularly, it can be observed that the value of \tilde{k}_2 must be limited and/or the value of $|R_{eq}|$ must be increased to ensure stability. This is a further indication that the use of an RC NC without compensation considerably limits the maximum attenuation

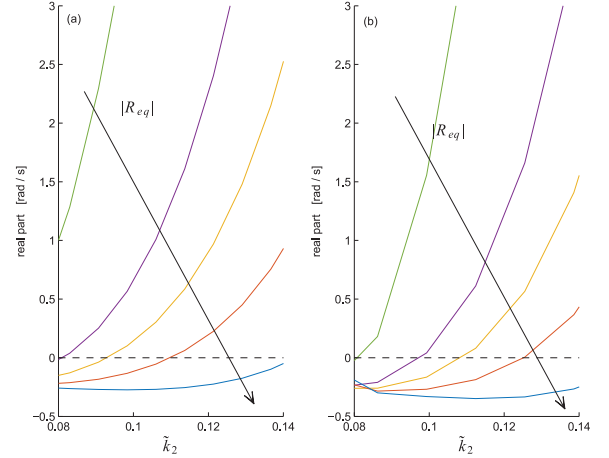


Figure 17. Trend of the real part of the pole related to the first mode, which can become unstable due to a low value of $|R_{eq}|$, as a function of \tilde{k}_2 . The system parameters are $\omega_1/(2\pi) = 30 \text{ Hz}$, $\omega_2/(2\pi) = 300 \text{ Hz}$, $\xi_1 = \xi_2 = 0.1\%$, $k_1 = 0.20$, and $k_2 = 0.05$ for an NC (a) in series and NCs (b) in SP with $\beta_{sp1} = 0.5$. Different values of R_{eq} are used: $-1, -5, -10, -20$ and $-50 \text{ M}\Omega$.

achievable because of instability problems, even if R_{min}^{opt} and L_{min}^{opt} are used in place of R_{num}^{opt} and L_{num}^{opt} .

A remarkable result provided by the SP configuration is shown in Figure 17(b). Here, we consider the same system as in Figure 17(a), but the SP configuration is used for the NC: here, the NC in series is built as an RC NC, while the parallel NC is an IC NC (see Berardengo et al., 2016b for more details). The comparison of Figure 17(a) and (b) indicates that the SP configuration improves the stability of the EMS compared to the series NC. Indeed, with the SP configuration, it is possible to use higher values of \tilde{k}_2 or poorer compensation (i.e. low $|R_{eq}|$ values) without causing instability.

Guidelines for coupling NCs to resonant shunt

All the previous analyses allow developing guidelines about how to apply shunt damping by coupling NCs and resonant circuits. Indeed, several choices are available for the NC connection and the layout of the link between R and L ; the previous analyses allow highlighting the best choice as a function of the specific application.

The first choice is related to the configuration between R and L . The series connection must be preferred when the EMEMCF is high because it offers better attenuation performance (see previously in the article the subsection related to the attenuation performance provided by IC NCs). When the EMEMCF is not high, the differences between the two connection types tend to become negligible (see the subsection related to the attenuation performance provided by IC

NCs). However, another point that must be taken into account is the practical implementation of L . It is often built using OP-AMPs because of its high value (Moheimani and Fleming, 2006; Thomas et al., 2012), and these circuits can generate additional resistances. When the series connection is considered, it is straightforward to compensate these resistive parasitic effects by changing R accordingly. Therefore, the series connection must be preferred.

For the NC layout, the choice depends on the considered frequency range. When high-order modes are taken into account, it is possible to choose between the parallel and the SP layouts. The parallel layout provides the advantage that IC NCs can generally be employed, while the SP layout can often require the use of RC NCs (for the NC in series). In the latter case, despite the presence of an RC NC, the circuit can be considered as ideal in terms of attenuation performance because the control is at high frequency (where the RC NC behaves as an IC NC). However, the stability is affected by the presence of an RC NC, and thus, the stability of the low-order modes must be checked. It follows that the use of the compensation resistance R_s is strongly encouraged if the stability must be improved.

With regard to low-order modes, the parallel NC typically provides low performance because the value of k_i cannot be greatly increased due to the stability limits. Hence, it is recommended to use either the series or the SP layout. Clearly, the SP layout allows improving the attenuation by some decibels compared to the series (or improving stability with the same attenuation performance). In both cases, if RC NCs have to be used, it is recommended to use the compensation resistance R_s for the same reasons explained before; if R_s is not used, a numerical minimisation procedure can often help to find the best values of R and L to enhance the attenuation performance. Furthermore, the SP layout should be preferred in the case of RC NCs because it improves the stability of the EMS.

Finally, when modes in the middle frequency range are taken into account, the SP shows performance and stability that are better than the series and the parallel layouts.

Generally, the use of the SP layout is suggested in almost all the cases, possibly coupled to the use of the compensation resistance R_s when RC NCs are used.

Experimental tests

This section presents the experimental tests conducted to validate the outcomes of the previous sections. The next subsection describes the set-up used for the tests. Then, the subsequent subsection validates the theoretical formulations derived for IC NCs, and the last subsection validates the results for RC NCs.

Experimental set-up

The set-up used consisted of a stainless steel cantilever beam (length 180 mm, width 30.5 mm and thickness 1.1 mm) with two piezoelectric patches (length 70 mm, width 30.0 mm and thickness 0.55 mm, material PIC 151) bonded at the cantilevered end. The two patches were electrically connected in series.

The structure was excited using a contactless actuator composed of a coil and a magnet bonded close to the beam tip (see Figure 18). Making current flow in the coil allowed exerting a force on the beam; this force was considered proportional to the current flowing in the coil (Thomas et al., 2003), which was measured using a current clamp. The response of the structure was measured using a laser Doppler velocimeter at a point close to the tip.

Eigenfrequencies and non-dimensional damping ratios were estimated through an experimental modal analysis with the piezoelectric patch short-circuited. The algorithm employed for modal parameter extraction was the polyreference least squares frequency-domain method (Peeters et al., 2004). The k_i values were estimated by measuring ω_i and $\hat{\omega}_i$ and using equation (10). The values of all these parameters will be provided explicitly for all the tests performed because the different tests were performed on different days, and thus, there were slight changes in the modal data.

For the C_{pi} values, we measured the trend of the capacitance of the piezoelectric patch C_{piezo} between 20 and 1400 Hz with a Hewlett-Packard 4284A LCR meter, and then, we interpolated the experimental points (see Figure 19 and Appendix 1). C_{piezo} is intended as $\underline{Q}(\Omega)/\underline{V}(\Omega)$, where $\underline{Q}(\Omega)$ and $\underline{V}(\Omega)$ are the complex amplitudes of Q and V , respectively, and the inherent resistance of the piezoelectric patch is neglected. This allowed us to estimate $C_{p1} = 40.16$ nF, $C_{p2} = 39.60$ nF, and $C_0 = 42.88$ nF. C_∞ was estimated by measuring the capacitance value at 100 kHz, and the result was 22.09 nF.

The NCs were built using Texas Instruments OPA445 OP-AMPs. The NC in parallel (as well as the

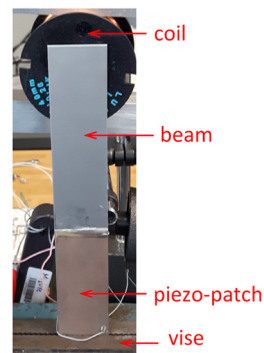


Figure 18. The experimental set-up.

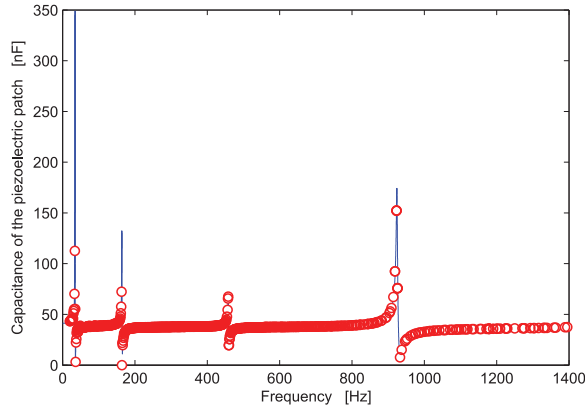


Figure 19. Trend of the modulus of the piezoelectric capacitance as a function of frequency. Points are related to experiments, while the line is the interpolated model.

NC in parallel in the SP layout) was built using the electrical scheme shown in Figure 14(b); we used the schemes shown in Figure 14(c) and (d) for the NC in series, as well as for the NC in series of the SP layout.

The inductance L was built using a synthetic circuit based on Antoniou's circuit (Thomas et al., 2012; Von Wangeheim, 1996) employing OP-AMPs OPA445 (see Appendix 3). The use of a synthetic circuit was due to the high inductance values in the different tests, which prevented the use of physical inductances. All the OP-AMPs were supplied with a direct current (DC) voltage of ± 30 V.

Experiments with ICs

This section discusses the tests performed on the first mode of the beam to validate the formulations derived for the values of ω_e^{opt} (see equation (21)), ξ_e^{opt} (see

equation (23)) and the corresponding A_{dB} value (see equation (26)). With regard to the tests with NC in parallel, an IC NC was used (see Figure 14(b) and test A column in Table 4). With regard to the tests with NCs in series and SP, we used an RC NC with the compensation resistance R_s for the NC in series (see Figure 14(d)); for the parallel NC in the SP layout, an IC NC was used (more details about the electrical connections for the SP can be found in Berardengo et al. (2016b, 2017)). The value of R_s was set to have a high value of $|R_{\text{eq}}|$ such that the RC NCs could be well approximated as IC NCs (see test B column for the series and test C column for the SP in Table 4). The tests were performed with L and R connected in series because this configuration offers higher attenuation levels compared to a connection in parallel (see previously in the article the subsection related to the attenuation performance provided by IC NCs). Appendix 3 shows, as an example, the circuit used for the tests with the series NC.

Figures 20 to 22 show the experimental results for NCs in parallel, series and SP, respectively, achieved by employing equations (21) and (23) for the shunt tuning. There is a satisfactory agreement between the theoretical expectations (equation (26)) and the experimental results. The curve related to the parallel NC (Figure 20) cannot be experimentally investigated for $\tilde{k}_i > 0.386$ because of the low instability threshold (theoretical instability for $\beta_1 > 0.55$ and experimental instability found at $\beta_1 = 0.55$, thus almost corresponding), as expected when using NC in parallel to control low-frequency modes (Berardengo et al., 2016b). For the instability with the series configuration of the NC, experimental instability was found at $\beta_2 = 0.90$, while the theoretical result would predict instability for $\beta_2 > 0.94$. Therefore, the stability conditions can be considered validated.

Table 4. Description of the parameters for the experimental tests.

Parameter	Test A	Test B	Test C	Test D
$\omega_1/(2\pi)$ (Hz)	34.42	34.45	34.50	34.40
$\hat{\omega}_1/(2\pi)$ (Hz)	35.58	35.65	35.65	35.60
k_1	0.2618	0.2662	0.2603	0.2664
ξ_1 (%)	0.39	0.36	0.36	0.33
C_1 (nF)	Changes	—	18.07	—
C_2 (nF)	—	Changes	Changes	Changes
R_{eq} (M Ω)	$-\infty$	−75.0	−75.0	−0.90 and −2.80
R_s (M Ω)	—	2.91	2.91	—
R_1 (k Ω)	11.47	Changes	11.47 (parallel) Changes (series)	Changes
R_2 (k Ω)	Changes	11.49	9.38 (parallel) 11.49 (series)	11.49
C (nF)	22.10	69.30	22.10 (parallel) 69.30 (series)	69.30
\hat{R} (M Ω)	—	Changes	Changes	Changes

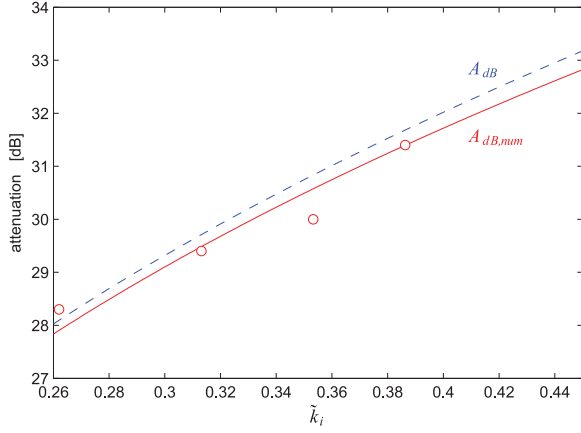


Figure 20. Comparison between experimental results (circles) and theoretical expectations (solid and dashed curves) for NC in parallel (Test A column in Table 4).

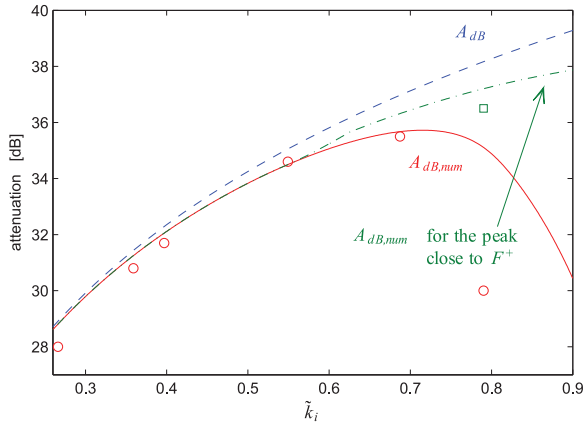


Figure 21. Comparison between experimental results (circles) and theoretical expectations (solid and dashed curves) for NC in series (Test B column in Table 4). The green dashed-dotted curve is related to the values of $A_{dB,num}$ considering only the peak of $|H_i|$ at high frequency (i.e. close to F^+) and neglecting the increase in the static gain of the FRF (see Figures 3(b) and 7); the square is the experimental point related to this $A_{dB,num}$ curve.

Note that during these tests, the circuit composed of the series connection of L and R was measured every time using a network analyser. Indeed, when an inductance is built using OP-AMPs, there is a possibility of having a parasitic resistance in series (Park and Inman, 2003; Viana and Steffen, 2006), as already mentioned. Therefore, we measured the entire circuit to stay as close as possible to the optimal values of the shunt inductance and resistance.

The only experimental points in Figures 21 and 22 where there is not a strict agreement with theory are those related to $A_{dB,num}$ (circles) at the highest \tilde{k}_i values. The reason for this result is that the maximum of the FRF amplitude is at very low-frequency values for these tests (i.e. approximately 2 Hz, see Figure 23) due

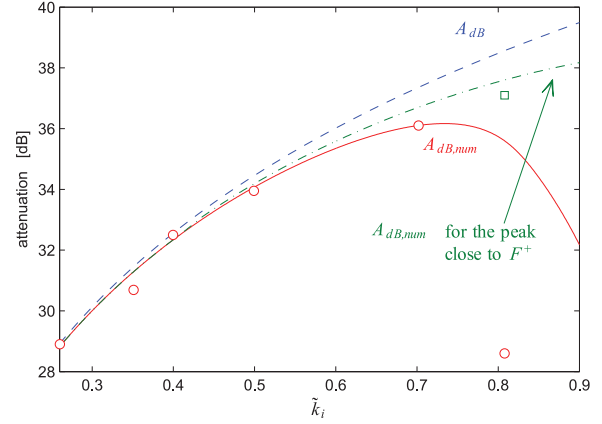


Figure 22. Comparison between experimental results (circles) and theoretical expectations (solid and dashed curves) for NCs in SP (Test C column in Table 4). The green dashed-dotted curve is related to the values of $A_{dB,num}$ considering only the peak of $|H_i|$ at high frequency (i.e. close to F^+) and neglecting the increase in the static gain of the FRF (see Figures 3(b) and 7); the square is the experimental point related to this $A_{dB,num}$ curve ($\beta_{sp1} = 0.45$).

to the increase in the static gain (see Figure 7). At such low-frequency values, the model used is expected to not be highly accurate because of different reasons, for example, we do not take into account the non-ideal behaviour of OP-AMPs and we neglect the leakage resistance of the piezoelectric patch (Doebelin, 2003; Okumura et al., 2014). However, the mentioned experimental points are able to properly describe the fact that the theoretical curves of $A_{dB,num}$ decrease for high \tilde{k}_i values. Furthermore, Figure 23 shows the increase in the FRF gain at low frequency for NCs in series with high β_2 values, as discussed in the subsection related to the attenuation performance provided by IC NCs (see also Figure 7).

According to the outcomes of the subsection related to the attenuation performance provided by IC NCs, we also know that the SP layout offers higher attenuation performance compared to the series and parallel layouts when the same β values are used. We also validated this result by performing a test with $\beta_1 = \beta_{sp1} = \beta_2 = \beta_{sp2} = 0.5$. The theoretical and experimental attenuation levels achieved match well. Indeed, Figure 24 shows the experimental FRFs achieved with the optimal L and R values (see equations (21) and (23)) for NCs in series, parallel and SP compared to the theoretical expectations.

Finally, some tests performed to validate the attenuation performance in mistuned conditions are shown. Figure 25 shows the comparison between experimental attenuations (blue circles in Figure 25) and the theoretical expectations (the isolines in Figure 25). Again, the agreement is good, thereby confirming the reliability of the theoretical model.

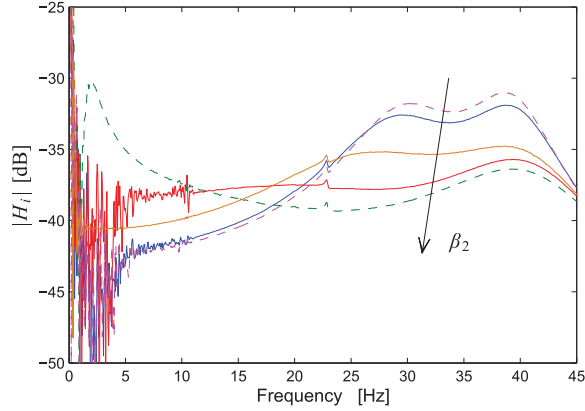


Figure 23. $|H_i|$ for IC NC in series (see Test B column in Table 4) for different β_2 (and thus \tilde{k}_i) values. The β_2 values are 0.45, 0.55, 0.765, 0.85 and 0.8865. The value of β_2 equal to 0.8865 corresponds to the experimental point (circle) with the highest value of \tilde{k}_i in Figure 21. The value of 0 dB corresponds to the FRF peak in SC.

Experiments with RCs

Figure 26 shows the comparison between the experiments and theory for an RC NC connected in series to the series of an inductance and a resistance. Different values of R_{eq} were tested. The data related to this test are presented in Test D column of Table 4. It is observed that the value of $|R_{eq}|$ is always low in these

tests (indeed, we are considering RC NCs here), and the compensation resistance R_s is not used.

In the test of Figure 26(a) (where $R_{eq} = -0.9 \text{ M}\Omega$), we have considered both the L and R values found through the theoretical formulae valid for IC NCs and the numerically optimal values found by means of numerical minimisation of the maximum of $|H_i^{\text{real}}|$. Using the theoretically optimal values with $R_{eq} = -0.9 \text{ M}\Omega$, the EMS is expected to become unstable for $\tilde{k}_i = 0.58$. Instability was found experimentally for $\tilde{k}_i = 0.59$. Therefore, good agreement is again found between theory and experiments. In addition, other values of R_{eq} (e.g. see Figure 26(b) where $R_{eq} = -2.8 \text{ M}\Omega$) showed good agreement between theory and experiments.

Another test (Test E, see Table 5; the values of the electrical parameters are almost the same of those provided in Table 4) was performed regarding the instability of RC NCs. The aim of this additional test is to show the benefit provided by the use of NCs in the SP configuration compared to the NC in series. In this case, the shunt impedance was tuned on the second mode of the beam (using L_{\min}^{opt} and R_{\min}^{opt}), and then, instability was checked for different values of R_{eq} and keeping the values of \tilde{k}_2 and \tilde{k}_1 constant (see Table 5). The instability check for the model was performed on the first two modes of the EMS by using equation (35); indeed, it was already explained previously that

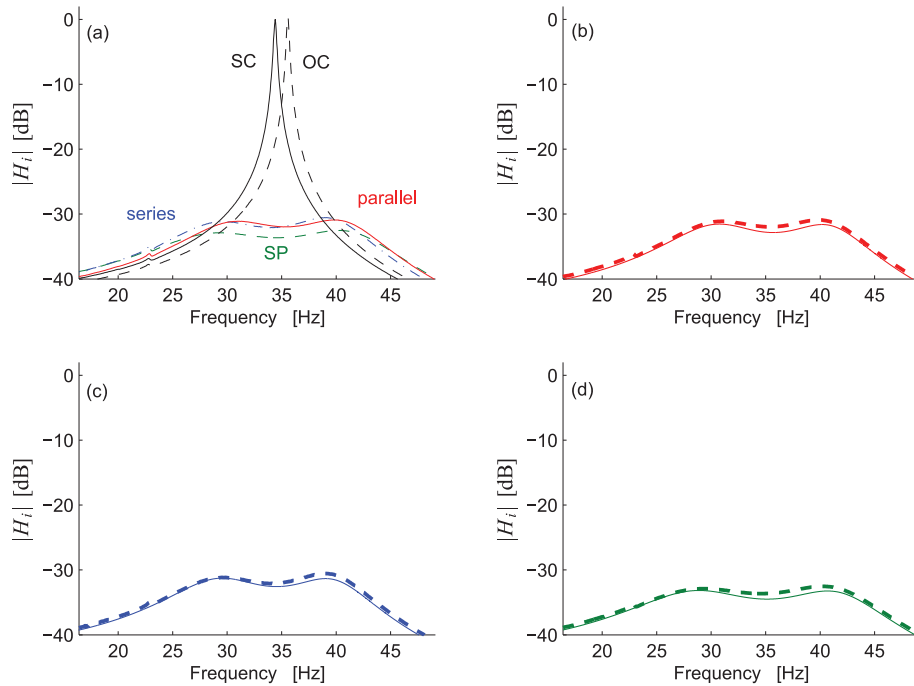


Figure 24. FRFs with IC NCs for $\omega_i/(2\pi) = 34.40 \text{ Hz}$, $\hat{\omega}_i/(2\pi) = 35.56 \text{ Hz}$, $\xi_i = 0.37\%$, $k_i = 0.2619$ and $\beta_1 = \beta_{\text{sp1}} = \beta_2 = \beta_{\text{sp2}} = 0.5$; R and L connected in series. (a) Experimental FRFs, (b) experimental (thick dashed line) and theoretical (thin solid line) FRFs for the NC in parallel, (c) experimental (thick dashed line) and theoretical (thin solid line) FRFs for the NC in series and (d) experimental (thick dashed line) and theoretical (thin solid line) FRFs for the NC in SP.

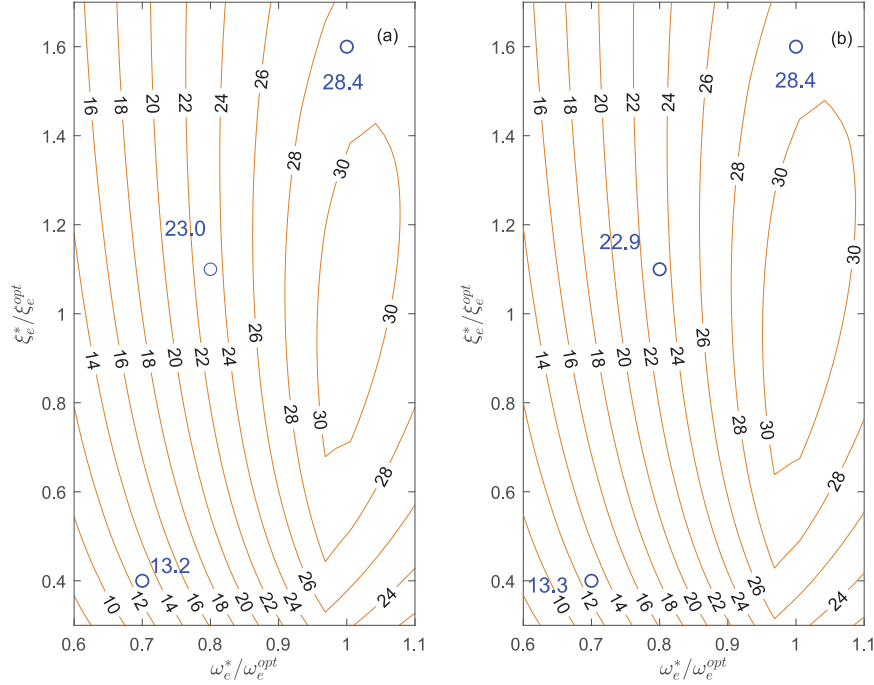


Figure 25. (a) $A_{dB,num}^{*,S,S}$ and (b) $A_{dB,num}^{*,S,P}$ for the beam with $\omega_i/(2\pi) = 34.40$ Hz, $\hat{\omega}_i/(2\pi) = 35.59$ Hz, $\xi_i = 0.36\%$, $k_i = 0.2653$ and $\beta_1 = \beta_2 = 0.5$. The iso-lines are the theoretical expectations, and the circles are the experimental points (the number close to each circle indicates the experimental attenuation). IC NCs are used (also using R_s).

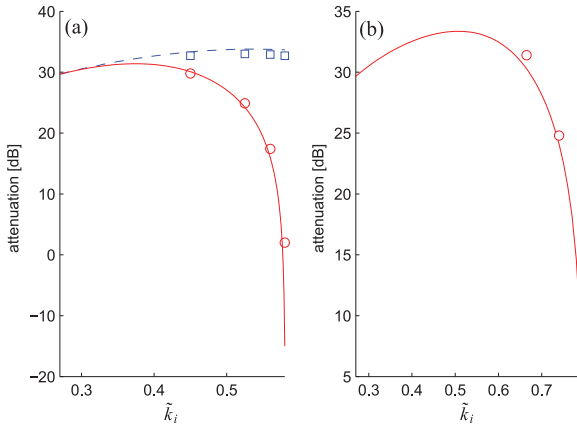


Figure 26. Trends of $A_{dB,real}$ (solid lines) and $A_{dB,min}$ (dashed line) for RC NC in series: (a) $R_{eq} = -0.9$ MΩ and (b) $R_{eq} = -2.8$ MΩ. Solid and dashed lines are related to the theoretical expectations; circles and squares are related to the experimental results for $A_{dB,real}$ and $A_{dB,min}$, respectively.

instability related to the use of RC NCs arises at low frequency.

Note that the FRF H_i^{real} related to NCs in the SP configuration can easily be derived through equation (35) by using $C_{pi} - C_1$ in place of C_{pi} , $k_i/\sqrt{1 - C_1/C_{pi}}$ in place of k_i and $\omega_i\sqrt{1 + k_i^2 C_{pi}/(C_{pi} - C_1)}$ in place of $\hat{\omega}_i$ (see Table 1). Indeed, the SP layout can be viewed as an enhanced version of an NC in series.

The use of the SP configuration allows decreasing the value of $|R_{eq}|$ more than the series before finding instability, which in turn means having a higher robustness to instability.

The comparison between the experimental and theoretical results is provided in Table 6, and the agreement is also good for this test, even if slight differences occur. Actually, in this test, slight changes in the values of the parameters involved (e.g. \tilde{k}_1 , \tilde{k}_2 and R) are able to significantly change the results. Therefore, it is expected that the uncertainty related to the measurement/

Table 5. Test E: modal data of the first two modes.

$\omega_1/(2\pi)$ (Hz)	$\hat{\omega}_1/(2\pi)$ (Hz)	ξ_1 (%)	k_1	\tilde{k}_1	$\omega_2/(2\pi)$ (Hz)	$\hat{\omega}_2/(2\pi)$ (Hz)	ξ_2 (%)	k_2	\tilde{k}_2
34.50	35.69	0.34	0.2649	0.8431	164.00	165.41	0.21	0.1314	0.3200

Table 6. Values of R_{eq} for which instability occurs in Test E (see Table 5).

Type of NC	Theoretical expectation	Experimental result
Series	−7.1 MΩ	−4.0 MΩ
SP with $\beta_{spl} = 0.45$	−4.8 MΩ	−3.5 MΩ
SP with $\beta_{spl} = 0.52$	−4.1 MΩ	−3.0 MΩ

estimation of the different parameters is able to explain these slight differences between the experimental and numerical results. However, the trends are similar for both experiments and theory, and the benefits provided by the use of the SP layout are demonstrated.

Conclusion

This article has addressed vibration damping by means of piezoelectric shunt. Specifically, the shunt layout taken into account is made from a resonant shunt coupled to NCs.

A common mathematical formulation has been shown to exist for all the possible layouts of the NCs (i.e. parallel, series and SP) regarding the optimisation of the shunt parameters and the consequent achievable vibration attenuation.

Since active elements (i.e. NCs) are considered in the shunt, stability conditions for the EMS have also been provided.

Furthermore, the behaviour of modified circuits, which cannot be considered as pure NCs but which must often be used in practical applications, has been analysed.

Finally, the advantages provided by the use of two NCs together, compared to traditional layouts where only one NC is used, have been highlighted in terms of both stability and attenuation performance.

All the mentioned analyses allowed developing some guidelines for facing different types of control problems to be provided, explaining how to improve performance and stability. The coupling between the classical resonant shunt and NCs is even able, in some cases, to provide an attenuation performance so high that resonance cancellation is achieved.

The theoretical results have been validated through an experimental campaign conducted on a cantilever beam coupled to a pair of piezoelectric patches.

Acknowledgements

The authors are grateful to Prof. Giovanni Chiorboli (Università degli Studi di Parma) for the support in the measurement of the capacitance of the piezoelectric patch.


Declaration of conflicting interests


The author(s) declared no potential conflicts of interest with respect to the research, authorship, and/or publication of this article.

Funding

The author(s) received no financial support for the research, authorship, and/or publication of this article.

ORCID iDs

Marta Berardengo  <https://orcid.org/0000-0002-8625-0822>

Stefano Manzoni  <https://orcid.org/0000-0002-9240-5472>

References

- Andreus U and Porfiri M (2007) Effect of electrical uncertainties on resonant piezoelectric shunting. *Journal of Intelligent Material Systems and Structures* 18: 477–485.
- Beck BS, Cunefare KA and Collet M (2013) The power output and efficiency of a negative capacitance shunt for vibration control of a flexural system. *Smart Materials and Structures* 22(6): 065009.
- Beck BS, Cunefare KA and Collet M (2014) Response-based tuning of a negative capacitance shunt for vibration control. *Journal of Intelligent Material Systems and Structures* 25(13): 1585–1595.
- Behrens S, Fleming AJ and Moheimani SOR (2003) A broadband controller for shunt piezoelectric damping of structural vibration. *Smart Materials and Structures* 12(1): 18–28.
- Berardengo M, Cigada A, Manzoni S, et al. (2015a) Vibration control by means of piezoelectric actuators shunted with LR impedances: performance and robustness analysis. *Shock and Vibration* 2015: 704265.
- Berardengo M, Manzoni S and Vanali M (2016a) The behaviour of mistuned piezoelectric shunt systems and its estimation. *Shock and Vibration* 2016: 9739217.
- Berardengo M, Manzoni S, Thomas O, et al. (2015b) A new electrical circuit with negative capacitances to enhance resistive shunt damping. In: *Proceedings of the ASME 2015 conference on smart materials, adaptive structures and intelligent systems (SMASIS 2015)*, Colorado Springs, CO, 21–23 September.
- Berardengo M, Thomas O, Giraud-Audine C, et al. (2016b) Improved resistive shunt by means of negative capacitance: new circuit, performances and multi mode control. *Smart Materials and Structures* 25: 075033.
- Berardengo M, Thomas O, Giraud-Audine C, et al. (2017) Improved shunt damping with two negative capacitances: an efficient alternative to resonant shunt. *Journal of Intelligent Material Systems and Structures* 28(16): 2222–2238.
- Collet M, Ouisse M, Cunefare K, et al. (2011) Vibroacoustic energy diffusion optimisation in beams and plates by means of distributed shunted piezoelectric patches. In: Vasques C and Rodrigues JD (eds) *Vibration and Structural Acoustics Analysis: Current Research and Related Technologies*. Dordrecht: Springer, pp. 265–302.

Date M, Kutani M and Sakai S (2000) Electrically controlled elasticity utilizing piezoelectric coupling. *Journal of Applied Physics* 87(2): 863–868.

De Marneffe B and Preumont A (2008) Vibration damping with negative capacitance shunts: theory and experiment. *Smart Materials and Structures* 17(3): 035015.

Den Hartog J (1956) *Mechanical Vibrations*. New York: McGraw Hill.

Doebelin E (2003) *Measurement Systems*. New York: McGraw-Hill.

Ducarne J, Thomas O and Deü J (2012) Placement and dimension optimization of shunted piezoelectric patches for vibration reduction. *Journal of Sound and Vibration* 331(14): 3286–3303.

Gopal M (2002) *Control Systems: Principles and Design*. 2nd ed. New Delhi, India: Tata McGraw-Hill Education.

Hagood N and Von Flotow A (1991) Damping of structural vibrations with piezoelectric materials and passive electrical networks. *Journal of Sound and Vibration* 146: 243–268.

Heuss O, Solloum R, Mayer D, et al. (2016) Tuning of a vibration absorber with shunted piezoelectric transducers. *Archive of Applied Mechanics* 86: 1715–1732.

Horowitz P and Hill W (1989) *The Art of Electronics*. 2nd ed. Cambridge: Cambridge University Press.

Kodejška M, Mokř P, Linhart V, et al. (2012) Adaptive vibration suppression system: An iterative control law for a piezoelectric actuator shunted by a negative capacitor. *IEEE Transactions on Ultrasonics, Ferroelectrics, and Frequency Control* 59(12): 2785–2796.

Liu K and Liu J (2005) The damped dynamic vibration absorbers: revisited and new result. *Journal of Sound and Vibration* 284: 1181–1189.

Manzoni S, Moschini S, Redaelli M, et al. (2012) Vibration attenuation by means of piezoelectric transducer shunted to synthetic negative capacitance. *Journal of Sound and Vibration* 331(21): 4644–4657.

Moheimani S and Fleming A (2006) *Piezoelectric Transducers for Vibration Control and Damping*. London: Springer-Verlag.

Neubauer M, Oleskiewicz R, Popp K, et al. (2006) Optimization of damping and absorbing performance of shunted piezo elements utilizing negative capacitance. *Journal of Sound and Vibration* 298(1–2): 84–107.

Okumura K, Takagi K, Inoue T, et al. (2014) Instability caused by parasitic resistances in piezoelectric shunt damping system with negative capacitance. In: *Proceedings of the SPIE 9057, active and passive smart structures and integrated systems 2014*, San Diego, CA, 9–13 March.

Park C and Inman D (2003) Enhanced piezoelectric shunt design. *Shock and Vibration* 10(2): 127–133.

Park CH and Baz A (2005) Vibration control of beams with negative capacitive shunting of interdigital electrode piezoceramics. *Journal of Vibration and Control* 11(3): 331–346.

Peeters B, Auweraer HVD, Guillaume P, et al. (2004) The polymax frequency-domain method: a new standard for modal parameter estimation? *Shock and Vibration* 11: 395–409.

Sluka T and Mokř P (2007) Feedback control of piezoelectric actuator elastic properties in a vibration isolation system. *Ferroelectrics* 351(1): 51–61.

Snowdon J (1968) *Vibration and Shock in Damped Mechanical Systems*. New York: Wiley.

Soltani P, Kerschen G, Tondreau G, et al. (2017) Tuning of a piezoelectric vibration absorber attached to a damped structure. *Journal of Intelligent Material Systems and Structures* 28(9): 1115–1129.

Tang J and Wang K (2001) Active-passive hybrid piezoelectric networks for vibration control: comparisons and improvement. *Smart Materials and Structures* 10(4): 794–806.

Thomas O, Deü JF and Ducarne J (2009) Vibration of an elastic structure with shunted piezoelectric patches: efficient finite-element formulation and electromechanical coupling coefficients. *International Journal of Numerical Methods in Engineering* 80(2): 235–268.

Thomas O, Ducarne J and Deü J (2012) Performance of piezoelectric shunts for vibration reduction. *Smart Materials and Structures* 21(1): 015008.

Thomas O, Touzé C and Chaigne A (2003) Asymmetric nonlinear forced vibrations of free-edge circular plates. Part II: experiments. *Journal of Sound and Vibration* 265(5): 1075–1101.

Viana F and Steffen V (2006) Multimodal vibration damping through piezoelectric patches and optimal resonant shunt circuits. *Journal of the Brazilian Society of Mechanical Sciences and Engineering* 28(3): 293–310.

Von Wangeheim L (1996) Modification of the classical GIC structure and its application to RC-oscillators. *Electronics Letters* 32(1): 6–8.

Yamada K, Matsuhisa H, Utsuno H, et al. (2010) Optimum tuning of series and parallel LR circuits for passive vibration suppression using piezoelectric elements. *Journal of Sound and Vibration* 329(24): 5036–5057.

Appendix I

The procedure for estimating C_{pi}

Appendix I explains how to estimate the value of C_{pi} . According to Berardengo et al. (2016b), the behaviour of the capacitance of the piezoelectric patch C_{piezo} as a function of frequency is as follows

$$C_{piezo}(\Omega) = C_{\infty} + \sum_{i=1}^N \frac{\chi_i^2}{\omega_i^2 + 2j\xi_i\omega_i\Omega - \Omega^2} \quad (44)$$

where j is the imaginary unit. C_{piezo} is intended as $\underline{Q}(\Omega)/\underline{V}(\Omega)$, where $\underline{Q}(\Omega)$ and $\underline{V}(\Omega)$ are the complex amplitudes of Q and V , respectively, and the inherent resistance of the piezoelectric patch is neglected.

If the trend of C_{piezo} is described only in the frequency range of the first m modes and if equation (10) is employed, the following expression is obtained (Berardengo et al., 2016b)

$$C_{piezo}(\Omega) = C_{pm} + \sum_{i=1}^m \frac{(k_i\omega_i\sqrt{C_{pi}})^2}{\omega_i^2 + 2j\xi_i\omega_i\Omega - \Omega^2} \quad (45)$$

According to Berardengo et al. (2016b)

$$C_{pi} = C_{pi+1} (1 + k_{i+1}^2) \quad (46)$$

Hence, if equation (46) is used in equation (45), the expression of C_{piezo} between the null frequency and a frequency value slightly higher than ω_m is a function of a single variable, which is C_{pm} (indeed, the other parameters of the expression can be estimated: ω_i and ξ_i by a modal analysis and k_i by employing the right-hand term of equation (10)). If such an expression is fitted with the experimental curve describing $C_{\text{piezo}}(\Omega)$ over the same frequency range by means of a minimisation procedure, the value of C_{pm} can be estimated. Then, using this value, the measured value of the k_i coefficients, and equation (46), the values of C_{pi} for the modes lower than the m th can also be estimated.

Appendix 2

Expressions of A_{dB} for the different layouts

Appendix 2 provides the expressions of A_{dB} (see equations (26) and (27)) as functions of ξ_i , \tilde{k}_i and k_i by using the expressions presented in Table 1.

With regard to R and L connected in series, the expression of $A_{dB}^{S,P}$ is

$$A_{dB} = 10 \log_{10} \frac{X_1 \sqrt{1 - \frac{1}{2 + k_i^2}}}{8\xi_i^2 \left[-8 - 7\tilde{k}_i^2 + 3\tilde{k}_i \sqrt{2(1 + \tilde{k}_i^2)} \right] (\xi_i^2 - 1)} \quad (47)$$

where

$$\begin{aligned} X_1 = & \left[-3\sqrt{2(2 + \tilde{k}_i^2)} + 16\xi_i\sqrt{3} \right] \tilde{k}_i^5 \\ & + \left[7\sqrt{2 + 3\tilde{k}_i^2 + \tilde{k}_i^4} - 8\xi_i\sqrt{6(1 + \tilde{k}_i^2)} \right] \tilde{k}_i^4 \\ & + \left[-3\sqrt{2(2 + \tilde{k}_i^2)} + 48\xi_i\sqrt{3} - 52\xi_i^2\sqrt{2(2 + \tilde{k}_i^2)} \right] \tilde{k}_i^3 \\ & + 8 \left[\sqrt{2 + 3\tilde{k}_i^2 + \tilde{k}_i^4} - 2\xi_i\sqrt{6(1 + \tilde{k}_i^2)} \right] \\ & + 10\xi_i^2\sqrt{2 + 3\tilde{k}_i^2 + \tilde{k}_i^4} \tilde{k}_i^2 + 8\xi_i \left[4\sqrt{3} - 7\xi_i\sqrt{2(2 + \tilde{k}_i^2)} \right] \\ & \tilde{k}_i + 64\xi_i^2\sqrt{2 + 3\tilde{k}_i^2 + \tilde{k}_i^4} \end{aligned} \quad (48)$$

The expression of $A_{dB}^{S,S}$ is

$$A_{dB} = 10 \log_{10} \frac{X_2 \sqrt{\frac{1 + k_i^2}{2 + 2k_i^2 - \tilde{k}_i^2}}}{8\xi_i^2 \left[8 + 8k_i^2 - \tilde{k}_i \left(\tilde{k}_i + 3\sqrt{2(1 + \tilde{k}_i^2)} \right) \right] (\xi_i^2 - 1)} \quad (49)$$

where

$$\begin{aligned} X_2 = & \left[\sqrt{(1 + k_i^2)(2(1 + k_i^2) - \tilde{k}_i^2)} - 8\xi_i\sqrt{6(1 + k_i^2)} \right] \tilde{k}_i^4 \\ & + \left[(3 - 4\xi_i^2)\sqrt{4(1 + k_i^2) - 2\tilde{k}_i^2} + 16\xi_i\sqrt{3} \right. \\ & \left. + k_i^2 \left(16\xi_i\sqrt{3} + 3\sqrt{4(1 + k_i^2) - 2\tilde{k}_i^2} \right) \right] \tilde{k}_i^3 \\ & - 8 \left[(2\xi_i^2 + k_i^2 + 1)\sqrt{(1 + k_i^2)(2 + 2k_i^2 - \tilde{k}_i^2)} \right. \\ & \left. - (2\xi_i k_i^2 + 2\xi_i)\sqrt{6(1 + k_i^2)} \right] \tilde{k}_i^2 \\ & + 8 \left[7(\xi_i^2 k_i^2 + \xi_i^2)\sqrt{4(1 + k_i^2) - 2\tilde{k}_i^2} \right. \\ & \left. - (4k_i^4 \xi_i + 8k_i^2 \xi_i + 4\xi_i)\sqrt{3} \right] \tilde{k}_i \\ & - 64\xi_i^2(1 + k_i^2)\sqrt{(2 + 2k_i^2 - \tilde{k}_i^2)(1 + k_i^2)} \end{aligned} \quad (50)$$

For $A_{dB}^{S,SP}$, its expression can be determined by noting that the SP can be viewed as an enhanced series NC thanks to the presence of the parallel NC.

With regard to R and L connected in parallel, the expression of $A_{dB}^{P,P}$ is

$$A_{dB} = 10 \log_{10} \frac{2\tilde{k}_i^3 + 8\xi_i\tilde{k}_i\sqrt{\tilde{k}_i(2 - \tilde{k}_i^2)}\sqrt[4]{2} + 8\xi_i^2(\sqrt{2} + \tilde{k}_i) + \sqrt{2}\tilde{k}_i^2(1 - 8\xi_i^2)}{8\xi_i^2(2\tilde{k}_i + \sqrt{2})(\xi_i^2 - 1)} \quad (51)$$

The expression of $A_{dB}^{P,S}$ is

$$A_{dB} = 10 \log_{10} \frac{-X_3}{8\xi_i^2(1 + k_i^2 - 3\tilde{k}_i^2)(\xi_i^2 - 1)} \quad (52)$$

where

$$\begin{aligned} X_3 = & 3\tilde{k}_i^6 - 4(1 + k_i^2 - 6\xi_i^2)\tilde{k}_i^4 \\ & + \left[12\xi_i^2\sqrt{2(1 + k_i^2 - \tilde{k}_i^2)} - 4\xi_i\sqrt{\tilde{k}_i(2 + 2k_i^2 - 3\tilde{k}_i^2)} \right. \\ & \left. + \sqrt[4]{8(1 + k_i^2 - \tilde{k}_i^2)} \right] \tilde{k}_i^3 \\ & + \left[(1 + k_i^2)(1 + k_i^2 - 32\xi_i^2) - 8\xi_i\sqrt{\tilde{k}_i(2 + 2k_i^2 - 3\tilde{k}_i^2)} \right. \\ & \left. + \sqrt[4]{2(1 + k_i^2 - \tilde{k}_i^2)^3} \right] \tilde{k}_i^2 \\ & + \left[4\xi_i(1 + k_i^2)\sqrt{\tilde{k}_i(2 + 2k_i^2 - 3\tilde{k}_i^2)} + \sqrt[4]{8(1 + k_i^2 - \tilde{k}_i^2)} \right. \\ & \left. - 4\xi_i^2(1 + k_i^2)\sqrt{2(1 + k_i^2 - \tilde{k}_i^2)} \right] \tilde{k}_i + 8\xi_i^2(1 + k_i^2)^2 \end{aligned} \quad (53)$$

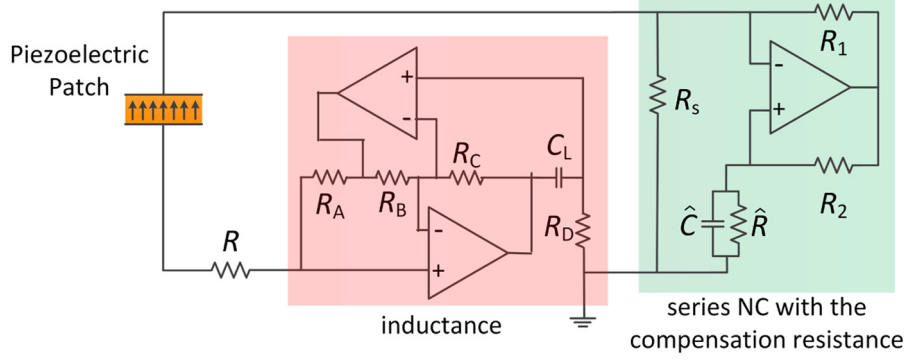


Figure 27. Layout of the circuit with R and L connected in series and an NC in series configuration, with the compensation resistance R_s . The inductance L is built using OP-AMPs.

With regard to $A_{dB}^{P,SP}$, it can easily be derived by noticing that the SP configuration can be seen as a series configuration enhanced by the use of the parallel NC.

Appendix 3

The implementation of the synthetic inductance

Appendix 3 explains the layout of the synthetic inductor built using Antoniou's circuit (Thomas et al., 2012; Von Wangeheim, 1996).

Figure 27 shows the inductance layout based on two OP-AMPs. This inductance is inserted in a global circuit. This circuit was that used in the tests with an NC in series using a compensation resistance. The connection between the inductance and the resistance R is in series.

Table 7. Parameter values used for the synthetic inductance.

R_A (k Ω)	R_B (k Ω)	R_C (k Ω)	R_D (k Ω)	C_L (μ F)
11.50	11.50	11.50	Potentiometer	4.98

According to Figure 27, a given inductance value is obtained by combining different resistances and a capacitance

$$L = \frac{C_L R_A R_C R_D}{R_B} \quad (54)$$

R_D was a potentiometer in these experiments for an easy tuning of the L value; the values of the other components are summarised in Table 7.